

**Nickel-Seeded Silicon Nanowires Grown on Graphene as Anode  
Material for Lithium-ion Batteries**

by

Abdel Rahman Elsayed

A thesis

presented to the University of Waterloo

in fulfillment of the

thesis requirement for the degree of

Master of Applied Science

in

Chemical Engineering

Waterloo, Ontario, Canada, 2014

© Abdel Rahman Elsayed 2014

## **Author's declaration**

I hereby declare that I am the sole author of this thesis. This is a true copy of the thesis, including any required final revisions, as accepted by my examiners.

I understand that my thesis may be made electronically available to the public.

## **Abstract**

There is a growing interest for relying on cleaner and more sustainable energy sources due to the negative side-effects of the dominant fossil-fuel based energy storage and conversion systems. Cleaner, electrochemical energy storage through lithium-ion batteries has gained considerable interest and market value for applications such as electric vehicles and renewable energy storage. However, capacity and rate (power) limitations of current lithium-ion battery technology hinder its ability to meet the high energy demands in a competitive and reliable fashion.

Silicon is an element with very high capacity to Li-ion storage although commercially impractical due to its poor stability and rate capabilities. Nevertheless, it has been heavily researched with more novel electrode nanostructures to improve its stability and rate capability. It was found that silicon nanomaterials such as silicon nanowires have inherently higher stability due to mitigation of cracking and higher rate capability due to the short Li-ion diffusion distance. However, electrode compositions based only on silicon nanowires without additional structural features and a high conductive support do not have enough stability and rate capability for successful commercialization. One structural and conductive support of silicon materials studied in literature is graphene. Graphene-based electrodes have been reported as material capable of rapid electron transport enabling new strides in rate capabilities for Li ion batteries.

This thesis presents a novel electrode nanostructure with a simple, inexpensive, scalable method of silicon nanowire synthesis on graphene nanosheets via nickel catalyst. The research herein shows the different electrode compositions and variables studied to yield the highest achievable capacity, stability and rate capability performance. The carbon coating methodology in addition

to enhancing the 3D conductivity of the electrode by replacing typical binders with pyrolyzed polyacrylonitrile provided the highest performance results.

## **Acknowledgements**

I would first like to thank my family and friends, especially my mother and my wife, for their tremendous support and patience with me.

The work reported herein was financially supported by General Motors and the University of Waterloo.

I would also would like to thank Dr. Fathy M. Hassan and Dr. Zhongwei Chen for their guidance and tremendous assistance in the Master's study.

Special thanks goes to the author's colleagues including, Hey Woong Park, Kun Feng, Dong Un Lee, Pouyan Zamani, Md. Ariful Hoque, Brian Kim, Victor Chabot, and Abdul Rahman Ghannoum for their assistance and support.

Furthermore, the author would like to acknowledge the important inputs of reviewers, including Dr. Aiping Yu and Dr. Michael Fowler.

# Table of Contents

Author's declaration.....	ii
Abstract.....	iii
Acknowledgements.....	v
List of Figures.....	ix
List of Tables.....	xii
List of Abbreviations.....	xiii
1. Introduction.....	1
1.1 Objectives and Motivations.....	3
1.2 Organization of Thesis.....	6
2. Background Information.....	7
2.1 Lithium ion batteries.....	7
2.1.1 Li ion battery principle.....	7
2.2 Silicon nanowires.....	10
2.2.1 Si NWs electrochemical properties: Why Si NWs for LIB?.....	11
2.2.2 Silicon nanowire synthesis method.....	11
2.2.3 Advantages of Nickel (Ni) over Gold (Au) in Li ion battery Applications.....	13
2.2.4 The Au-Si system versus Ni-Si system.....	14
2.3 Graphene.....	17
3. Materials synthesis and characterization.....	20

3.1	SiNW on Graphene synthesis.....	20
3.1.1	GO synthesis .....	20
3.2	Material Characterization Techniques .....	23
3.2.1	Scanning electron microscopy .....	23
3.2.2	Transmission electron microscopy .....	25
3.2.3	X-ray diffraction .....	26
3.2.4	Raman Spectroscopy.....	28
3.2.5	Thermogravimetric Analysis .....	29
3.1.6	Electrode preparation technique .....	30
3.1.7	Coin cell assembly .....	31
3.1.8	Battery cycler .....	32
3.1.9	Cyclic Voltammetry.....	33
3.1.10	Electrochemical Impedance Spectroscopy .....	34
3.2	Structural and chemical characterization of optimal batch .....	36
3.2.1	Morphology Characterization .....	36
3.2.2	Chemical identification.....	38
3.2.3	Mass ratio determination – TGA .....	42
4.	Electrode fabrication and testing .....	43
4.1	Effect of increasing Si NW content.....	43
4.1.1	Purpose of study.....	43

4.1.2	Experimental .....	43
4.1.3	Results and discussion .....	44
4.2	Effect of carbon coating .....	48
4.2.1	Purpose of this study .....	48
4.2.2	Experimental .....	48
4.2.3	Results and discussion .....	48
4.3	Effect of binder .....	51
4.3.1	Purpose of this study .....	51
4.3.2	Experimental .....	52
4.3.3	Results and discussion .....	53
4.4	Further analysis of optimal batch SiNW-G-PPAN .....	58
4.4.1	Rate capability analysis .....	58
4.4.2	EIS analysis .....	60
4.4.3	TEM after testing .....	61
5.	Summary and Future Work .....	62
5.1	Recommendation for Future Work .....	63
7.	References .....	66

## List of Figures

Figure 1: Comparing the energy density of different types of batteries <sup>4</sup> .....	3
Figure 2: Illustration of forming the SiNW-G material .....	6
Figure 3: Illustration of a common Lithium Ion cell undergoing charge .....	8
Figure 4: Au-Si Phase Diagram <sup>34</sup> .....	15
Figure 5: The Nickel-Silicon phase diagram <sup>37</sup> .....	16
Figure 6: Si nanowire growth from a) gold seed undergoing VLS and b) nickel seed undergoing VSS .....	17
Figure 7: (a) Starting graphite powder and (b) resulting Graphitic Oxide (GO) powder .....	21
Figure 8: Experimental Apparatus and Steps in synthesis procedure.....	22
Figure 9: Powder samples of (a) G-NiNPs and (b) SiNW on G-NiNPs.....	23
Figure 10: SiNW-G material casted on copper foil with doctor blade .....	30
Figure 11: Coin cell dimensions .....	31
Figure 12: Illustration of coin cell components. (Coin cell size is 2 cm wide and 3.2 mm thick) .....	32
Figure 13: Equivalent circuit for a Lithium-ion cell with SEI formation (adapted from Reddy et al. <sup>57</sup> ).....	34
Figure 14: Example Nyquist plot corresponding to the equivalent circuit in Figure 13 <sup>57</sup> .....	35
Figure 15: Illustration of optimal batch of carbon coated SiNW-G with PPAN to enhance 3D conductivity of the electrode.....	36
Figure 16: (a) SEM image of NiNPs on graphene and (b) Higher resolution SEM of NiNPs on Graphene .....	37

Figure 17: a) SiNW grown on graphene (SiNW-G), b) TEM image of SiNW-G, c) HAADF-TEM (High-Angle Annular Dark-Field) of SiNW-G, and d) High Resolution TEM (HRTEM) of C-coated SiNW and the inset is the FFT diffraction pattern .....	38
Figure 18: (a) HAADF-TEM of SiNW-G with EDX elemental mapping of the elements (b) Si, (c) Ni, (e) C, and (f) O and all elements in (d).....	39
Figure 19 (a) XRD of SiNW-G and (b) NiNPs-G .....	40
Figure 20: Raman spectroscopy of (a) SiNW on graphene and (b) Carbon-coated SiNW on graphene.....	41
Figure 21: TGA of SiNW-G .....	42
Figure 22: SEM images of low loading SiNW-G.....	44
Figure 23: Electrochemical data of non-carbon coated SiNW-G with NaCMC binder, low Si content batch. (a) Voltage profile (b) Low rate (0.1 A/g) cycling (c) rate capability.....	45
Figure 24: Graphene completely covered with high loading of SiNW.....	47
Figure 25: (a) cycle data and (b) voltage profile of non-carbon coated high loading SiNW on G with NaCMC.....	47
Figure 26: SEM image of (a) G-NiNPs and (b) Carbon coated Si NWs on Graphene.....	49
Figure 27: (a) cycling and (b) voltage profile of C-coated SiNW with NaCMC .....	50
Figure 28: Self-standing electrodes of C-coated SiNW-G .....	52
Figure 29 (a) cycling and (b) voltage profile of C-coated, self-standing SiNW-G .....	54
Figure 30: Electrochemical performance of SiNW-G-PPAN showing (a) First 5 cycles at 0.1 A/g b) remaining cycles at 0.1 A/g (c) Voltage profile and (d) CV profile.....	55
Figure 31: (a) Voltage profile and (b) Cycle data of Graphene reference material at 0.1 A/g.....	56

Figure 32: SiNW-G-PPAN battery performance for (a) rate capability cycling, (b) rate capability V profiles, (c) cycling at 1.7 A/g after 5 cycles conditioning, and (d) cycling at 6.8 A/g after 5 cycles conditioning ..... 59

Figure 33: Rate capability comparison with SiNW-G, SiNW without G, and G reference ..... 59

Figure 34: EIS data after (a) first discharge of SiNW-G and (b) 100th discharge for SiNW-G, SiNW and G electrodes..... 60

Figure 35 (a) TEM image, (b) HAADF-TEM image, (c) HRTEM image and EDX mapping of (d) Si (e) C and (f) O for G-SiNW electrode material after 100 discharge/charge cycles..... 61

## List of Tables

Table 1: Reference XRD data for Ni (left) and Si (right).....	28
---	----

## List of Abbreviations

LIB	Lithium-Ion Battery
SiNW	Silicon nanowires
NiNP	Nickel nanoparticle
GO	Graphene oxide
G	Graphene
SEM	Scanning electron microscopy
TEM	Transmission electron microscopy
EDX	Energy Dispersive X-Ray Spectroscopy
XRD	X-Ray Diffraction
CV	Cyclic Voltammetry
EIS	Electrochemical Impedance Spectroscopy
TGA	Thermogravimetric Analysis
NaCMC	Sodium Carboxymethylcellulose
PAN	Polyacrylonitrile
C-coated	Carbon-coated
EC	Ethylene Carbonate
DMC	Dimethyl Carbonate
FEC	Fluoroethylene carbonate
SEI	Solid Electrolyte Interphase
C rate	Charge rate

## **1. Introduction**

The current world energy economy is heavily dependent on fossil fuels and non-renewable sources which are increasingly unsustainable and unfavorable due to a number of reasons. The continued increase in demand for oil paradoxically combined the rapid depletion of non-renewable oil resources is not promising for the future of energy. Air pollution due to fossil fuel emissions (e.g. CO<sub>2</sub>) causes climate change and contaminating the air that society breathes. Water pollution through oil spills and petrochemical waste causes contamination of our water resources which in turn raises the energy demands due to the increasing need for water treatment facilities.

All these concerns, among others, were sufficient to generate enough interest for cleaner ways to meet our demands through energy storage and conversion without toxic emissions or stress on the environment. The dominant way to store chemical energy and convert it to various forms for human use such as electrical (electric power grid) and kinetic (transportation) is through fossil fuels. In urban centers, human transportation using automobiles is a very significant source of fossil fuel emissions and it dominates the different modes of transportation that exist today. Replacing the internal combustion engine (ICE) with a battery-powered electric motor in electric vehicles (EVs) would enable zero emission transportation.<sup>1</sup> Power systems based on sustainable energy sources instead of burning fossil fuels is also very desirable for the same benefit of minimizing harmful emissions.<sup>2</sup>

However, the limitations of current battery technologies have allowed only hybrid electric vehicles (HEVs) and plug-in hybrid electric vehicles (PHEVs) to be widely commercialized. HEVs and PHEVs have both an ICE and a battery-powered electric motor so it still can release greenhouse gases, but nevertheless the hybrid system enables efficient fuel utilization with reduced emissions. Even then, the cost and performance limitations of current batteries in commercialized HEVs and PHEVs leave lots of room for much needed improvement.

Renewable energy sources, such as wind and solar, require highly efficient energy storage systems to be able to store and deliver energy on demand to enhance their ability to compete with fossil fuel based energy systems.<sup>3</sup>

Lithium (Li) ion batteries are among the most promising candidates for this required improvement in energy storage due to their superior energy density in comparison with other battery chemistries such as nickel metal hydride (NiMH) and lead acid batteries. This is illustrated in Figure 1 below.

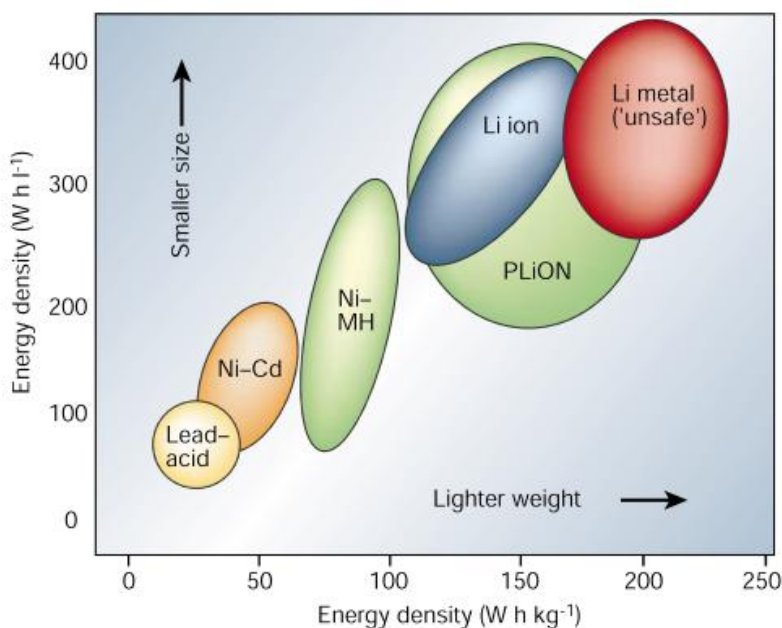


**Figure 1: Comparing the energy density of different types of batteries** <sup>4</sup>

Both gravimetric (per mass) and volumetric (per volume) charge density of lithium ions are superior to all other compounds used in batteries. However there are some bottlenecks that still prevent the large scale commercialization of Li ion batteries for EVs and renewable energy storage, which are hoped to be addressed in this research. <sup>5</sup>

## 1.1 Objectives and Motivations

This project aims to address some of the limitations of commercial LIBs with a novel electrode nanostructure. The first limitation is the limited capacity of the commercially available graphite-based LIBs that require massive weights of batteries in order to meet the energy needs of EVs and renewable energy storage. This bolsters the costs of such batteries making commercialization even more difficult. Secondly, safety concerns due to the flammability of both graphite electrodes and the electrolyte at high temperature make it difficult to use for applications where a lot of internal heating occurs, particularly in applications such as EVs.

Despite the improvement of cooling systems and safety mechanisms in laptop computers, for example, companies still issue recalls of batteries due to their safety issues.<sup>6</sup>

Thirdly, they suffer from poor performance at high currents (rate of charge/discharge) which makes them impractical when high power is needed, and this relates to the poor rate capability of the graphite material whereby critical loss in capacity is observed upon significantly increasing the charge/discharge rate of the battery.<sup>7</sup>

Silicon (Si) is a promising replacement to graphite due to its high capacity (4200 mAh g<sup>-1</sup> theoretical maximum); over ten times that of graphite (372 mAh g<sup>-1</sup>)<sup>8</sup> and also its stronger resistance to flammability. However, Si suffers from poor stability due to the high volume changes (> 300%) associated with the alloying mechanism in the lithiation of silicon as opposed to the intercalation mechanism in graphite (only 10%). These volume changes cause structural collapse and loss of electrical contact to both the current collector and conductive additives in the composite material leading to rapid capacity decay over subsequent charge/discharge cycles. Furthermore, silicon is a semiconducting material which, if used without conductive support, suffers from poor capacity and rate capability due to the lack of electrical pathways for charge carriers.

Many routes have been investigated to overcome these challenges. Various polymer binders have been demonstrated to be a stabilizing factor helping enhance the structural stability of the Si-based electrode through hydrogen bonding with the silicon surface.<sup>9</sup> Introducing porosity to the silicon material was also found to accommodate the volume changes improving stability of the material, but also reducing the diffusion distance of Li ions allowing for higher charge/discharge

rates.<sup>10</sup> Using nanomaterials (such as Si nanoparticles and nanowires) has been found to mitigate propagation of cracks from mechanical stress and hence have inherently higher stability<sup>11</sup>.

Nano-sized silicon materials, such as Si NWs, were found to have shorter Li-ion diffusion distance and hence have higher rate capabilities. However, relying only on faster Li-ion diffusion is not sufficient. The rapid transport of electrons also contributes to the improved rate capability, and this was achieved through highly conductive additives such as carbon nanotubes and graphene nanosheets.<sup>12-14</sup>

Furthermore, coating the silicon with a conductive material, such as amorphous carbon, was found to improve the coulombic efficiency of the silicon-based electrodes because of protecting the silicon active material from direct exposure to the electrolyte.<sup>15</sup>

In this project, a novel electrode nanostructure is proposed whereby silicon nanowires (Si NW) are directly grown on graphene nanosheets by simple chemical vapor deposition (in atmospheric pressure) with the assistance of Nickel (Ni) nanoparticles (NPs) as a catalyst for growth. By growing Si NW on graphene, a direct path is provided for electric conduction to allow a synergistic improvement of rate capability through both the short diffusion distance of Li ions through Si NWs and the rapid transport of electrons on the graphene surface. Furthermore, by decorating the graphene sheets with well dispersed Ni NPs, it provides a template for growing well dispersed Si NWs preventing them from agglomerating together and hence, providing a buffer for volume change during charging and discharging to improve the stability. Using Ni instead gold (Au), which is the more common catalyst for SiNW growth, means a significant

reduction in cost and also avoiding some issues associated with Au in the battery as shall be discussed later. An illustration of the SiNW-G material is shown in the figure below.

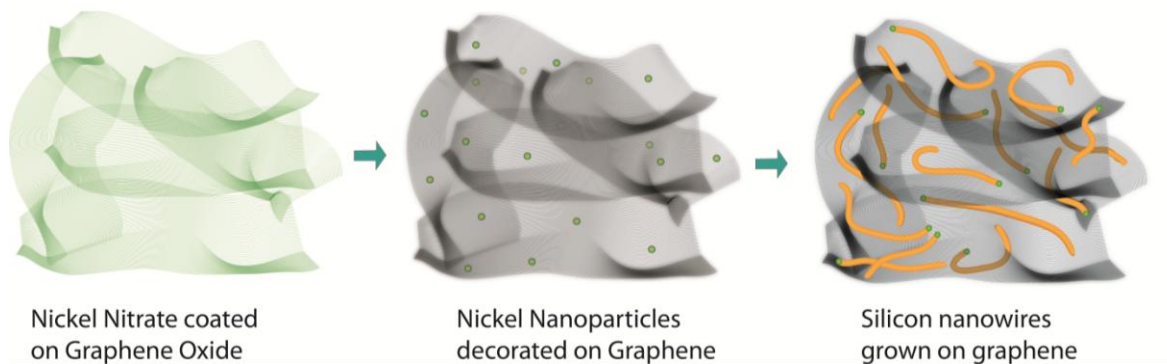


**Figure 2: Illustration of forming the SiNW-G material**

## 1.2 Organization of Thesis

This thesis which explores the optimal performance achievable with the SiNW-G electrode nanostructure is divided into five sections. Section 1, which is this one, introduces the topic with the overview of the objectives of this research and the importance of this work in addressing some limitations of LIBs with a novel electrode nanostructure. Section 2 is intended to provide the necessary background information and literature review of the theory behind the LIB operation, and the properties and synthesis methodologies of both SiNWs and Graphene. Section 3 provides the background information regarding the equipment used for synthesis and material characterization. Both sections 2 and 3 are intended to provide a solid foundation to be able to understand the results discussed in the sections that follow. Section 4 discusses the electrochemical testing techniques and results of electrochemical testing with different electrode compositions, and concluding with the optimal electrode composition. Finally, section 5 provides a summary of this project and a discussion on the future direction of this work.

## **2. Background Information**

### **2.1 Lithium ion batteries**

#### **2.1.1 Li ion battery principle**

Batteries are energy systems that contain one or more electrochemical cells which convert stored chemical energy to electrical energy. Lithium-Ion Battery (LIB) is a class of rechargeable batteries that use lithium reactions in both positive and negative electrodes which can reversibly host and release lithium ions, as illustrated by Figure 3 below. They were preceded by lithium batteries which utilize metallic lithium instead of a lithium host. Lithium batteries were found to be unsafe due to dendrite formation over the lithium metal after a few cycles that eventually cut through the separators and cause a short-circuit.<sup>4</sup> Lithium-Ion Batteries, on the other hand, use a lithium compound as a cathode material (such as Lithium Cobalt Oxide, shown as  $\text{Li}_{x-1}\text{CoO}_2$  in the figure) which is inherently safer without dendrite formation issues.

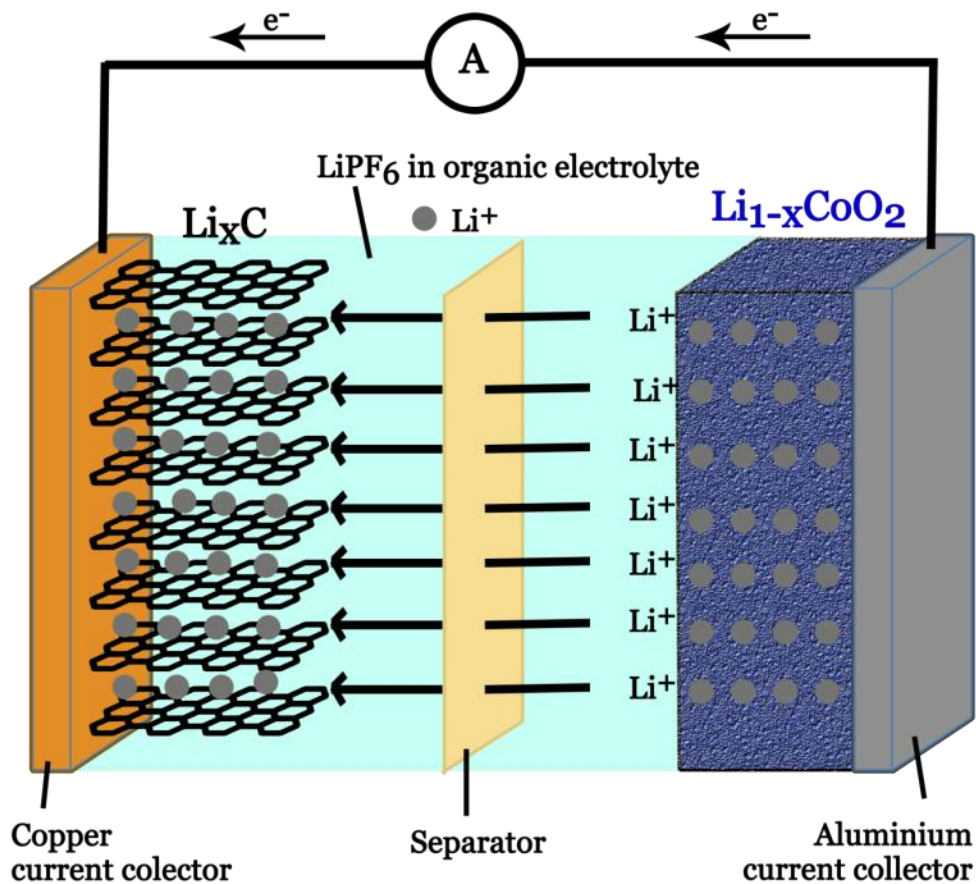
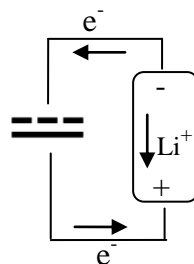
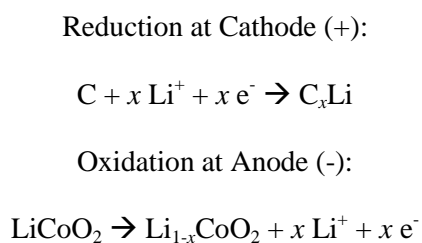


Figure 3: Illustration of a common Lithium Ion cell undergoing charge

The most commonly used anode in the LIB industry is a carbon graphite anode (shown as  $\text{Li}_x\text{C}$  in the figure above).

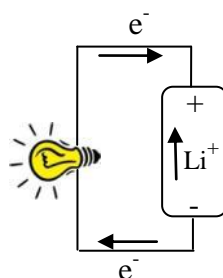
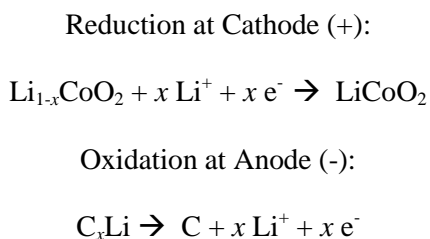
When a cell is manufactured, it is initially at a discharged state with  $\text{LiCoO}_2$  at the cathode and graphite (C) at the anode. Energy is then stored in the battery by charging it using an external power source.

During charging, as a current is applied through an external power supply, the graphite electrode (C) becomes the cathode (+) where reduction occurs, and the  $\text{LiCoO}_2$  electrode becomes the anode (-) where oxidation occurs, as illustrated with the redox reactions below:



**Charging**

Now the battery is ready to be used as a power source to release the energy stored to a load (such as a light bulb). This time, the  $Li_{1-x}CoO_2$  electrode behaves as the cathode (+) and the lithiated graphite ( $C_xLi$ ) electrode behaves as the anode (-). (Graphite anode and Lithium cobalt oxide cathode is the naming convention used in the battery industry). The following redox reactions take place when the circuit is closed with a load (e.g. light bulb), leading to current flow:



**Discharging**

What drives the discharge is the electromotive force (EMF) due to the excess electrons found in the unstable lithiated graphite ( $C_xLi$ ) which have a high drive to lose those electrons. In addition, the positive charge generated after the  $LiCoO_2$  lose electrons to become  $Li_{1-x}CoO_2$  makes it more energetically favorable to gain electrons, and that too has its own EMF. The potential difference across the positive and negative terminals is also known as the EMF. The combined EMF for a typical Li ion battery made from graphite and  $LiCoO_2$  is  $3.6 V$ <sup>16</sup>, which explains why commercial Li ion cells commonly provide between 3 to 4 V, and a battery made of 4 cells for a laptop computer would provide 12 V.

As the battery is discharged, the potential difference keeps decreasing due to charge neutralization, and the battery is “depleted” when that potential difference reaches zero and the initial state of the material is restored. The battery is then ‘recharged’ by using an external power supply as done initially to oxidize the  $\text{LiCoO}_2$  and reduce the graphite and so on and so forth. One cycle is completed after a full charge and discharge are done, and a battery’s ability to retain capacity over several cycles is a measure of its stability, also known as capacity retention.

Large loads require more current to be drawn from the battery, and the discharge/charge rate will therefore increase and the battery will deplete faster (smaller time,  $t$ ). If the capacity of the battery (relates to the energy,  $E$ ) does not drop too much after increasing the current drawn, this means it has a high rate capability, and can deliver high amounts of power ( $P = E/t$ )

The standard representation of the rate capability of the battery is through the charge rate (C rate). The C rate is based on the time it takes for a full charge to occur, and it can be calculated based on the current applied and maximum reversible capacity. For example, if the reversible capacity of the composite is 2000 mAh/g, then 1C would be a current density of 2000 mA/g, and 0.1C would be 200 mA/g. For 1C at 2000 mA/g it would take 1 hour to reach the maximum capacity (usually less than 1 hour due to the capacity drop associated with increasing the rate), and for 0.1C rate it would take 10 hours to reach the maximum capacity. If the full silicon capacity is considered (4200 mAh/g) then 1 C would be equivalent to 4200 mA/g.<sup>13</sup>

## **2.2 Silicon nanowires**

Silicon nanowires (Si NWs) are cylindrical/wire morphologies of silicon usually below 100 nm in diameter and several  $\mu\text{m}$  in length. The first publication of silicon wire growth was by

Treuting and Arnold in 1957<sup>17</sup> at a time when they were commonly referred to as ‘silicon whiskers’ or ‘filamentary silicon’ and often much larger than 100 nm in diameter. What features Si NWs can provide for LIBs and the synthesis method will be discussed in the following section.

### **2.2.1 Si NWs electrochemical properties: Why Si NWs for LIB?**

Nanostructured Si materials such as Si NWs and Si NPs have several advantages over bulk Si materials in terms of electrochemical properties. Firstly, the nano-sized diameters have shorter Li-ion diffusion distance and higher resistance to crack propagation<sup>18</sup>, allowing for more efficient charge transport and higher mechanical stability (respectively).

The 1D nano-structure of Si NWs is what sets them apart from Si NPs. The advantage can be clearly realized when the direct growth of vertically aligned Si NWs on conductive templates have enabled even higher efficiency of charge transport due to the improved electrical contact and even further reduction of Li-ion diffusion pathways. One example of this is Si NWs directly grown on stainless steel current collector as developed by Chan et al.<sup>19</sup>

### **2.2.2 Silicon nanowire synthesis method**

There are two main approaches of preparing silicon nanowires: the bottom up approach and the top down approach. The bottom-up approach, which was the approach first used in history, involves the growth of wires on a nano-sized catalyst (or ‘seed’) where silicon preferentially deposits and grows in a Chemical Vapor Deposition (CVD) setup.<sup>20</sup> This catalyst is usually a metal nanocrystal on a substrate as per the Vapor-Liquid-Solid (VLS)<sup>21</sup> or Vapor-Solid-Solid

(VSS)<sup>22</sup> mechanisms, but it can also be silicon oxide nucleation sites formed in situ at high temperature as per the Oxide Assisted Growth (OAG) mechanism.<sup>23, 24</sup> The Supercritical Fluid - Liquid - Solid (SFLS) mechanism has also been used which replaces the gas phase with a liquid at supercritical temperature and pressure.<sup>25</sup> This is a solution-based synthesis of SiNWs which is easier to scale up for industrial scale production and hence garnered some research interest.

The top-down approach usually involves the chemical etching of silicon substrates creating void channels that leave behind nanowire morphologies. This is achieved through metal-assisted (electroless) or anodic (electrical) etching with Hydrofluoric Acid (HF).<sup>26</sup> However, this approach involves costly consumption of material and the use of costly and environmentally toxic etchants like HF, and it cannot be used for the direct synthesis of silicon nanowires on graphene and hence does not fit the goal of this research.

In VLS growth of Si NWs, the vapor phase contains a silicon precursor such as Silane, SiH<sub>4</sub>, or silicon tetrachloride, SiCl<sub>4</sub>. If SiCl<sub>4</sub> is used, a reducing agent, usually H<sub>2</sub> gas is also needed to produce silicon and give off HCl as a by-product. It is also known as Chemical Vapor Deposition (CVD) of SiCl<sub>4</sub>, in which the following reaction occurs:<sup>27</sup>



Other research reports have used vaporized zinc as a reducing agent instead of H<sub>2</sub> which is less expensive and simultaneously functions as the seed catalyst for the wire growth.<sup>28</sup> However this

was found to not be suitable for this project because it would be difficult to homogeneously distribute non-agglomerated zinc seeds on the graphene nanosheets that way, and this would make it difficult to yield well-dispersed silicon nanowires on graphene. It was determined that it's best to first synthesize well dispersed metal nanoparticles on graphene prior to silicon nanowire growth. There are enough reports on dispersed metal nanoparticles on graphene which show that the preparation method is simple and very successful.<sup>29-32</sup>

In addition, it was determined that the  $\text{SiCl}_4 + \text{H}_2$  system would be most suitable due to safety concerns that were found with  $\text{SiH}_4$  which required specialized equipment to be able to work with  $\text{SiH}_4$  safely that were not available.

The following sections will describe the advantages of using Nickel catalyst instead of Gold for SiNW growth and a detailed discussion about the growth mechanism.

### **2.2.3 Advantages of Nickel (Ni) over Gold (Au) in Li ion battery Applications**

The most commonly used metal for Si NW growth is gold, Au, because of its high resistance to oxidation and lower temperature required for Si NW growth compared to other metals. Furthermore, the use of Au in the electronics industry has been quite well established with cost-effective performance. However, it would be erroneous to assume that the same thing is applicable for the Li-ion battery industry.

In addition to its high cost, gold has been found to be undesirable for the Li-ion batteries<sup>33</sup> due to its capacity loss effect, especially at higher charge/discharge rates, which would work counterproductively with the goal of achieving high rate capability material. This problem can be

avoided by adding a gold etching step before using in the battery, but that adds more cost and complication to the process.

On the other hand, nickel (Ni) is a much cheaper material that is commonly used in high performance energy storage devices such as fuel cells, supercapacitors and batteries. More specifically it has also been studied with both silicon<sup>13</sup> and graphene<sup>29</sup> in Li-ion battery anodes with performance-boosting features. This also removes the need for any Ni etching steps which would otherwise add more complication and cost to the process. Furthermore, synthesis of Ni NPs is much easier and cost-effective than Au NP synthesis. No sputtering techniques or lengthy reflux reactions are required.<sup>29</sup>

#### **2.2.4 The Au-Si system versus Ni-Si system**

For VLS growth with the Au-Si system, the reaction temperature must be above the eutectic which is 363 °C as shown in the phase diagram below.

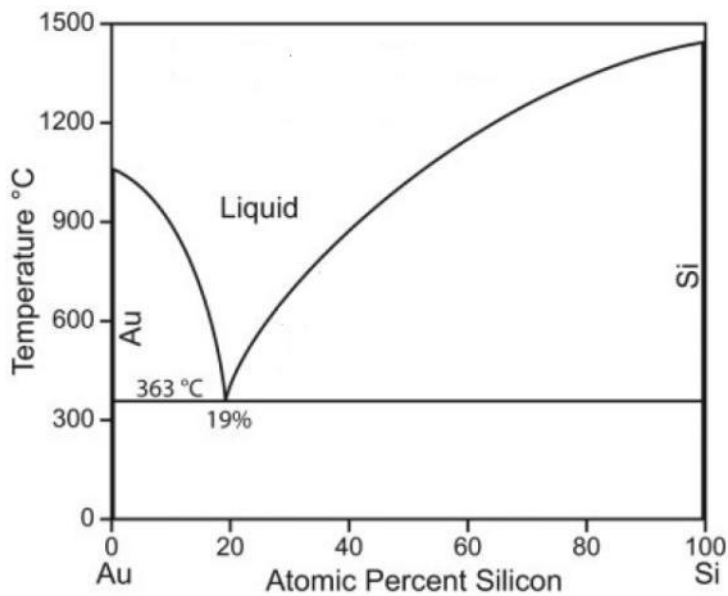


**Figure 4: Au-Si Phase Diagram** <sup>34</sup>

For the  $\text{SiCl}_4$  precursor, higher temperature is required to also break the Si-Cl bonds and hence typically it is done above 800 °C (the Si-H bonds in  $\text{SiH}_4$  are weaker and hence can be broken at lower temperatures. This partially explains the reason for  $\text{SiH}_4$  being more unstable and dangerous to work with than  $\text{SiCl}_4$ ).

The Au seed catalyzes the above reaction making the silicon preferentially deposit on the Au seeds forming Au-Si alloy NPs which become liquid when the Si portion is around 15 % (atomic). As the Si portion increases, the solid silicon phase starts forming and it keeps growing at the Au-Si interface resulting in wire formation, as illustrated in Figure 6 a) below.

The eutectic point for the Si-Ni system is 993 °C which is much higher than that of the Au-Si system as shown in Figure 5. However the Ni-Si phase diagram has many more phases including silicide phases below the eutectic point. These silicide phases give the opportunity of enabling silicon wire growth below the eutectic point where the seed particles are still in the solid phase.<sup>35</sup>

This is referred to as Vapor-Solid-Solid (VSS) growth.<sup>22</sup> This phenomenon was also observed with the Ti-Si system which has similar properties with Ni in terms of SiNW growth.<sup>36</sup>

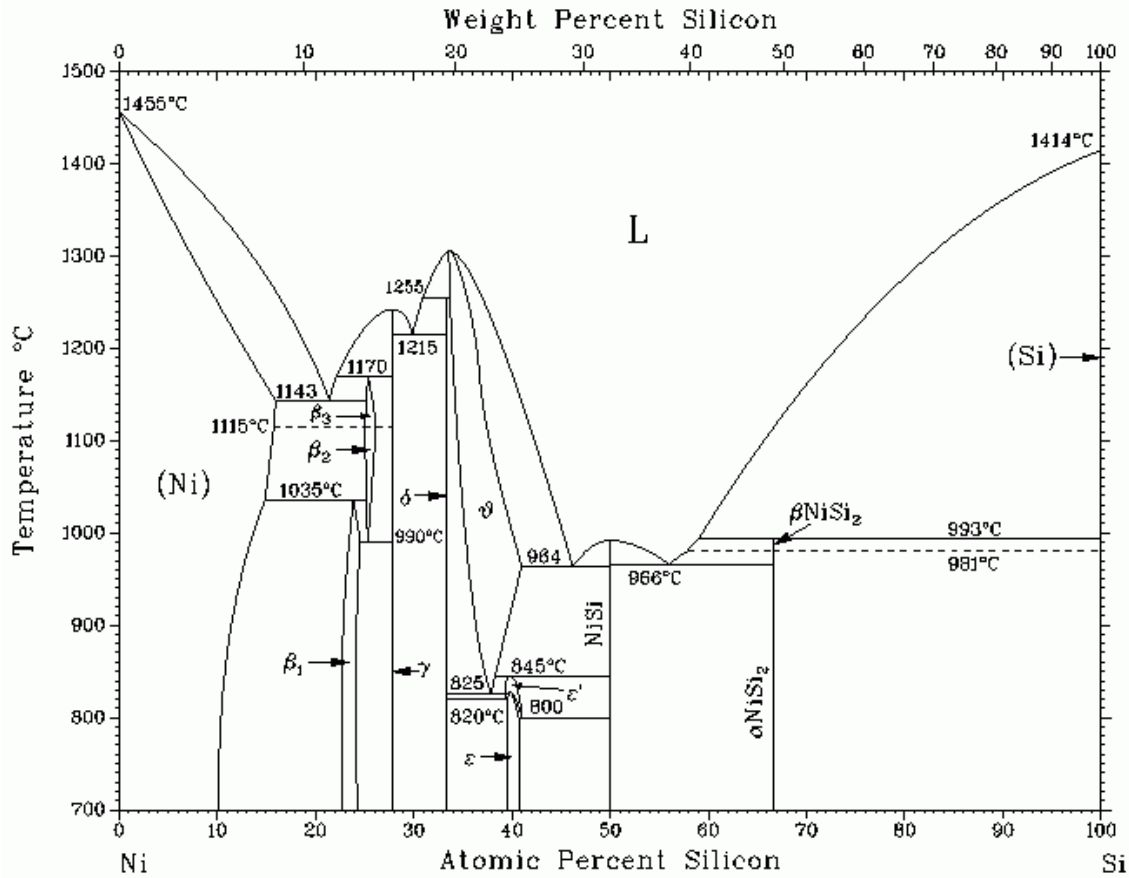
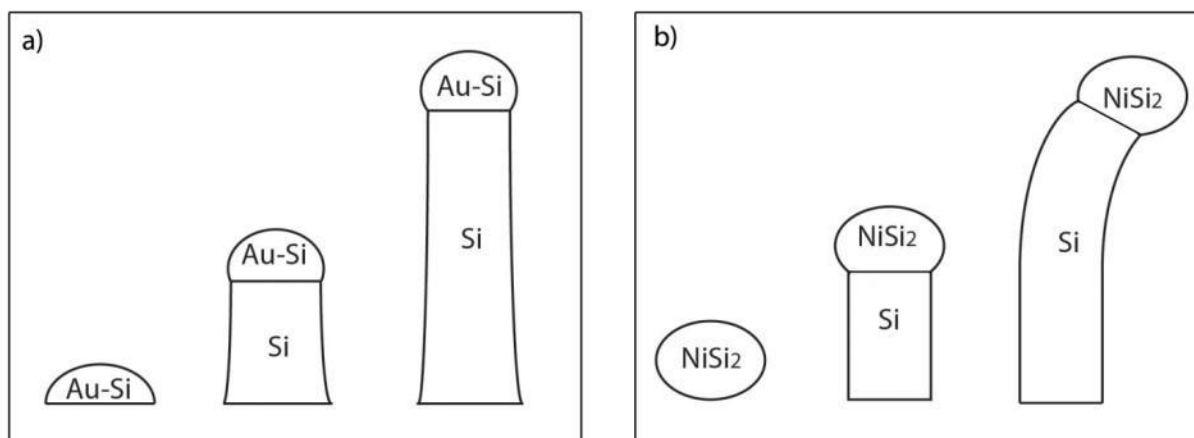


Figure 5: The Nickel-Silicon phase diagram<sup>37</sup>

The main advantage of using lower temperatures is that it allows smaller wire diameters because at higher temperatures the Ni NP seed increase in size due to Ostwald ripening. Zhang et al. found that 900°C was the optimal temperature for Si NW growth using Ni NP catalyst and  $\text{SiCl}_4 + \text{H}_2$  system.<sup>38</sup>

It is important to note that such VSS grown wires were found to contain more crystal defects which tend to yield more randomly oriented nanowires as opposed to straight nanowires<sup>21</sup> (as

illustrated in Figure 6 b). Having crystal defects is a concern if the Si NWs are to be used in an electronic device, but that is not the case in an electrochemical cell where the Si material becomes amorphous anyway after the first cycle. Ensuring that the surface of Si NWs are well attached to the surface of a graphene nanosheets was determined to be more important for improved electrical contact, and that would be better achieved with smaller nanowires that are compatible with the size of the graphene nanosheets, and hence VSS growth of Ni-seeded Si NW at 900°C was used for this work.



**Figure 6: Si nanowire growth from a) gold seed undergoing VLS and b) nickel seed undergoing VSS**

### 2.3 Graphene

Graphene is a single layer of hexagonally-arranged  $sp_2$  carbon atoms. Graphene layers are most commonly found in nature stacked in the form of graphite, which is a well known carbon-based electrical conductor. It was found that exfoliating graphite to isolate the graphene layers boosted the electrical and thermal conductivity of the material. Graphene has much higher electron mobility ( $200000 \text{ cm}^2 \text{ V}^{-1} \text{ s}^{-1}$ ) than graphite ( $20000 \text{ cm}^2 \text{ v}^{-1} \text{ s}^{-1}$ ) which has attracted interest for electrical applications.<sup>39</sup> For Li-ion batteries, a high electron mobility contributes to better rate capability. Graphene can show much better performance than graphite at higher charge/discharge rates due to these reasons.<sup>40</sup>

Another attractive aspect of graphene, theoretically, is that it can take lithium ions from both sides, and this a strong reason for it having higher capacity than other carbon-based materials such as carbon nanotubes.<sup>41</sup> The capacity contribution of graphene, besides the structural and electrical support, also adds more benefit for LIBs.

Several research groups investigated graphene support with silicon as anode material for Li ion batteries.<sup>42-46</sup> However, they separately synthesize silicon then physically mix it with graphene as opposed to directly growing silicon nanowires on graphene. Nevertheless, the reported advantages include enhancing the reversible capacity of silicon due to enhanced accessibility to Li ions and improving the stability due to accommodating the volume expansion of the silicon.

It was generally found that increasing the graphene content improves the stability but with the cost of sacrificing capacity and first cycle coulombic efficiency. The capacity of graphene is lower than silicon as previously discussed, but also it has inherently lower first cycle coulombic efficiency due to the fact that Li ions get trapped into the defect sites in graphene which does not occur with silicon.<sup>42</sup> Therefore, usually an optimal ratio of silicon and graphene are usually investigated to maximize capacity and first cycle efficiency while maintaining stability.<sup>45</sup>

One of the drawbacks of graphene, most significant for LIB, is that the very high conductivity is only in 2D. When considering 3D electrode designs, some inter-sheet electronic pathway could also be considered. Evidently, research has been done to incorporate carbon nanotubes with graphene to improve its performance for LIB.

There are different ways of producing graphene, the method used in this research is the chemical modification of graphite to graphitic oxide followed by thermal reduction to graphene, also known as reduced graphene oxide. This method was deemed to be the most suitable to deposit well-defined and distributed Ni NPs as a suitable template for silicon nanowire growth. It was also found to have the most attractive scalability due to the solution-based synthesis.<sup>47</sup>

### **3. Materials synthesis and characterization**

#### **3.1 SiNW on Graphene synthesis**

To fabricate well dispersed nickel nanoparticles on graphene, graphene oxide (GO) was first synthesized by the modified hummer's method<sup>47</sup>, followed by mixing with nickel nitrate hexahydrant, then SiCl<sub>4</sub> CVD. Each process is described in detail in the following.

##### **3.1.1 GO synthesis**

5g graphite powder is mixed with 900 mL concentrated H<sub>2</sub>SO<sub>4</sub> and 100 mL concentrated H<sub>3</sub>PO<sub>4</sub> in a conical flask and stirred for 30 minutes. 45 g of KMnO<sub>4</sub> are slowly added and mixed for additional 15 minutes. The temperature is raised to 50 °C and left to stir for 16 hours at 1200 rpm. The oil bath is then replaced with an ice bath to cool down the solution, and 1L of DDI water is slowly added. 50 mL of H<sub>2</sub>O<sub>2</sub> is then added and the final solution is centrifuged and washed with DDI water, HCl, ethanol and finally DDI water again until the solution reaches pH 7. The final solution was then freeze dried to obtain GO powder. This was based on the modified hummer's method.

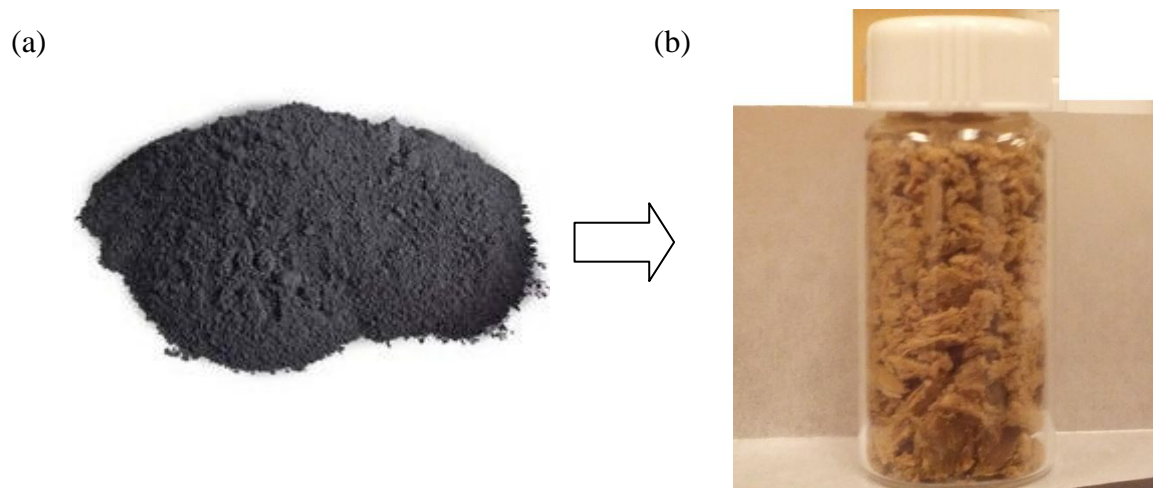


**Figure 7: (a) Starting graphite powder and (b) resulting Graphitic Oxide (GO) powder**

### **Graphene-Ni NPs and SiNW synthesis**

Nickel nitrate hexahydrant,  $\text{Ni}(\text{NO}_3)_2 \cdot 6\text{H}_2\text{O}$ , 0.1 M 250  $\mu\text{L}$  was then added to 150 mg GO dispersed in water and the mixture was sonicated for 1 hour then left to dry at 60 °C under magnetic stirring. The GO-Nickel Nitrate material was then heated to 700 °C under Argon atmosphere for 1 hour inside the furnace system illustrated in Figure 8 below (but without the  $\text{SiCl}_4$  injected yet). The temperature was then increased to 900 °C and  $\text{H}_2$  gas was for purged for 30 minutes at 500 sccm.

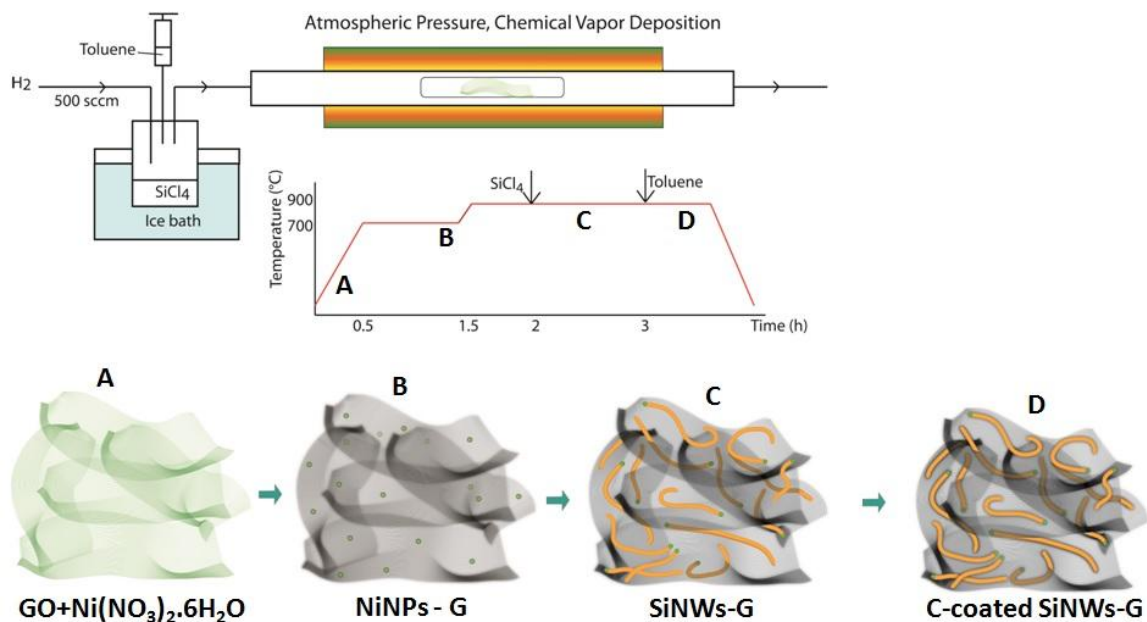


**Figure 8: Experimental Apparatus and Steps in synthesis procedure**

$SiCl_4$  precursor was then injected into the bypass setup. Typically, 300  $\mu L$  of  $SiCl_4$  is injected for 15 mg of Graphene/Ni. After the  $SiCl_4$  is completely depleted, toluene can be then injected (typically 50  $\mu L$  for 300  $\mu L$  of  $SiCl_4$ ) if a carbon coating is required. The furnace was then left to cool down after the reaction was complete.

Toluene was chosen due to three main reasons: 1) it can vaporize easily and get carried by the carrier gas into the CVD system, 2) it selectively deposits amorphous carbon layers to cover the Si surface due to pi-bond interaction, and 3) there are no oxygen or water by products during thermal decomposition of toluene which would otherwise cause unwanted reactions or oxidation on the Si surface.<sup>48, 49</sup> Benzene is another alternative carbon precursor with very similar properties and has also been used in silicon carbon coating.<sup>50</sup> Figure 9 below shows the sample after heat treatment without  $SiCl_4$  CVD and after  $SiCl_4$  CVD.

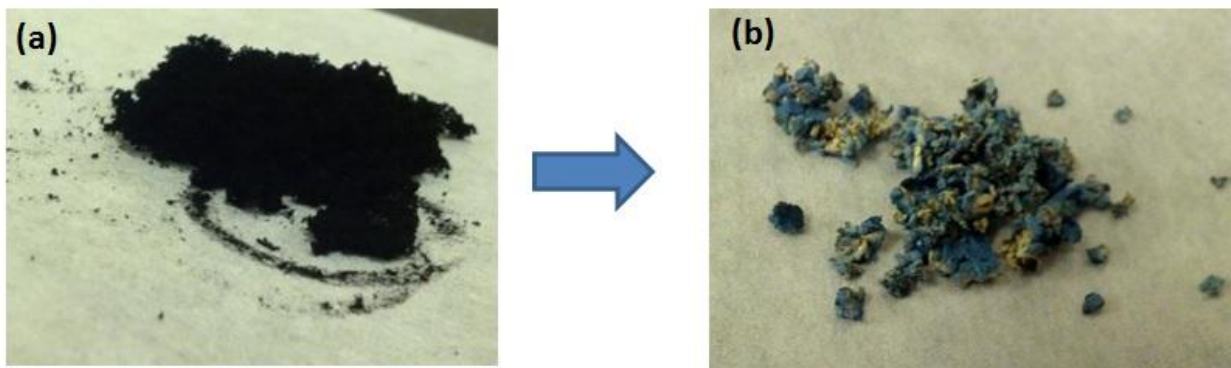


**Figure 9: Powder samples of (a) G-NiNPs and (b) SiNW on G-NiNPs**

## **3.2 Material Characterization Techniques**

### **3.2.1 Scanning electron microscopy**

Scanning electron microscopy (SEM) was used to study the morphology of the SiNW-G material at the submicron and  $>10$  nm scale. It is a useful technique with simple sample preparation and fast equipment operation. The only limitation is that samples must be conductive. For non-conductive samples, such as polymers, gold coating is required which makes sample preparation more complex, but this is not an issue for the SiNW-G material.

Electron interaction with the sample is the basis for SEM operation. A primary electron is emitted from an emission source, and a beam of electrons is generated due to the potential difference between the source and cathode. The electron beam energy typically ranges from 0.2 kV to 40 kV. Several magnetic segments focus this electron beam travelling through a column to achieve different spot sizes (typically 0.4 nm to 5 nm) for different resolutions.

As the electron beam hits the sample, two main types of electrons are emitted: Secondary and Backscattered electrons. Secondary electrons are generated from the primary electrons causing ionization of the sample, and this occurs very close to the surface of the sample. Secondary electrons therefore carry **surface topology** information to investigate the morphology of the sample. Backscattered electrons, on the other hand, are generated from (inelastic) scattering of the primary electrons by the nuclei of atoms in the sample, which carry information about the atomic number of elements in the sample. Together, both secondary and backscattered electrons are used to generate the SEM images.

In order to construct an SEM image, the electron beam is scanned over the sample area to be imaged in a line-by-line fashion and scattered electrons are detected with varying signal strengths reflecting different surface topologies.

X-rays can also be emitted due to the interaction of the primary electron beam with the sample, and therefore X-Ray detectors can also be installed with the SEM equipment enabling element identification. This part of the SEM machine is commonly referred to as Energy Dispersive X-ray Spectroscopy (EDX).

Specifically in this work, SEM was used to confirm the presence of nanowire morphologies attached to exfoliated graphene sheets.

### 3.2.2 Transmission electron microscopy

Transmission electron microscopy (TEM) was used to study the SiNW-G material with higher resolution. High resolution TEM can actually be used to measure lattice spacing of material and differentiate crystalline surfaces from amorphous surfaces which is very useful to characterize amorphous coatings due oxides or carbon.

The sample preparation for TEM requires dilute dispersion of the sample in a solvent like ethanol or methanol and transferring a very thin layer of material on specialized copper grids. It is much more sensitive to contamination than SEM and hence requires more care and time to prepare.

Like SEM, TEM is also based on electron interaction with the sample. A primary electron beam is also generated in the same way like SEM except with much higher kinetic energy ranging from 100 kV to 400 kV. The magnetic segments in the TEM column are capable of forming spot sizes in the angstrom scale.<sup>51</sup>

The higher energy electron beam for TEM penetrates the sample much deeper. Some electrons are scattered while others go right through the sample. To image the sample, contrast information is provided by the difference in energy from electrons after the primary electron beam hits the sample. The crystal structure of materials can be imaged with the higher energy electrons because the interactions occur with both the valence electrons in the atomic shell and the atomic nuclei.

TEM has more capabilities over SEM such as the selected area electron diffraction (SAED) studies and Electron Energy Loss Spectroscopy (EELS). With shorten wavelengths of TEM these techniques can provide addition information regarding material composition and chemical bonding. EDX can also be carried out due to the presence of X-ray but with greater accuracy. This is especially useful when supported with colored mapping of each element giving very conclusive information regarding the distribution of elements on the material being imaged.

Finally, one of the strongest features of TEM if it has even higher resolution capabilities, referred to as High Resolution TEM (HRTEM). This technique allows the imaging of crystal lattice of the sample and it operates through the interference of primary electron beams (wave property).

Specifically, in this work TEM was used to confirm the Ni seeded SiNW growth mechanism by differentiating the Si segment from the Ni particle which was difficult to do with SEM alone. It was also used to reveal the carbon coating which is an amorphous layer that can be differentiated from the crystalline silicon layer at high resolution. EDX was also used alongside the TEM image to further confirm the elements silicon, nickel and carbon and their distribution on the nanomaterial.

### **3.2.3 X-ray diffraction**

X-ray diffraction (XRD) is a common technique used for chemical identification and obtaining information regarding the crystal structure of the sample. XRD was primarily used in this study to confirm that the intended pure silicon nanowires were formed instead of other material or

silicon compounds such as silicon carbide or silicon oxide which have different crystallographic information and signature XRD patterns. It would be very difficult to do that by relying only on EDX element identification technique provided with SEM and TEM.

The XRD operation principle relies on radiating X-rays on the sample which interacts with the atoms and lattice spaces between the atoms, and this is possible due to the small wavelength of X-rays. This provides information on the order of atoms, or the lack thereof. The sample is fixed on a base, called goniometer, upon which the X-rays are radiated as it rotates in a pre-set range of angles. Diffraction of X-rays occur at certain angles, called the Bragg angles, where the distance traveled by the X-rays reflected from lattice planes differs by an integer number,  $n$ , of wavelengths.<sup>52</sup> Constructive interference occurs, leading to the formation of diffraction patterns with varying intensity at different Bragg angles. The XRD result plots the intensity versus the angle, and signature patterns can be used to identify the material present. A table of Silicon and Nickel signature patterns are provided below.

**Table 1 Reference XRD data for Ni (left) and Si (right)** <sup>53</sup>

Ni			Si		
d (Å)	hkl	2θ	d (Å)	hkl	2θ
3.524	100	25.27	3.13552	111	28.443
2.492	110	36.04	1.92011	220	47.303
2.035	111	44.52	1.63747	311	56.123
1.762	200	51.89	1.35722	400	69.131
1.576	210	58.57	1.24593	331	76.377
1.439	211	64.78	1.10857	422	88.032
1.246	220	76.44	1.04517	511	94.954
1.175	300	82	0.96005	440	106.71
			0.91799	531	114.094
			0.8587	620	127.547
			0.8282	533	136.897

The hkl numbers are conventional representations of unique lattice planes, each plane corresponding to different inter-atomic lattice spacing, d.

Different monochromatic X-Ray sources can be used for different X-Ray energies. The XRD machine used in this project generates Copper K- $\alpha$  X-ray radiation, which has a wavelength of 1.54 Å. With this information, the lattice spacing for silicon can be calculated, governed by the equation below.

$$2 * d * \sin(2\theta) = \lambda \quad (2)$$

Specifically, in this work XRD was used to confirm that the synthesized material is pure silicon and not other silicon compounds such as silicon oxide or silicon carbide, which would be difficult to determine through EDX-supported TEM alone. It was also used to confirm the nanoparticles on graphene were indeed nickel nanoparticles and not nickel oxide.

### **3.2.4 Raman Spectroscopy**

The operation of Raman Spectroscopy is based on scattering of monochromatic light. Inelastic scattering from different materials give useful information for chemical identification and specifically for carbon materials it can determine the structural character of graphitic carbons and stresses on core materials coated with carbon shell. Typically, a compound light microscope is used with a monochromatic light beam. A normal light source is used when the sample is being fixed on the stage of the microscope and image focusing is done. After aligning and focusing on the sample is complete, the chamber is closed and the normal light source is turned off so that only the monochromatic light source radiates on the sample. Photons absorbed by the sample cause the molecules to vibrate, rotate, and bend with different states, which correspond to different wavelengths of inelastic scattered light.<sup>54</sup> A filter is used to remove the elastic scattered

light, and a detector is used to receive signals from inelastic scattered light. The intensity of emitted light versus the wavenumber ( $\text{cm}^{-1}$ ) is plotted, and the resulting spectrums can be compared with signature reference spectrums for material identification. Shifting of reference wavenumber values can occur due to external stresses which may be identified to reveal core-shell structures.<sup>55</sup> This was used to confirm the presence of carbon coating shell on the silicon nanowires. Furthermore, the presence of graphene nanosheets, instead of graphite, was also determined by the characteristic band patterns that differentiate graphene from graphite powder.

Specifically, in this work Raman Spectroscopy was used to confirm the carbon coating on silicon through the peak shifting effect, and also characterize the graphene after the SiNW deposition.

### **3.2.5 Thermogravimetric Analysis**

Thermogravimetric Analysis (TGA), as its name suggests, is a simple technique which operates by monitoring the mass changes of a sample with temperature. This can be done in either nitrogen or air, with varying heating rates and maximum temperature. TGA is useful to determine the mass ratio of material in a composite. For this project, carbon materials can be totally burned off in air at high temperature while the silicon material remains. This was used to accurately determine the amount of graphene present in the SiNW-G composite. Fast heating rate of  $25^\circ\text{C}/\text{min}$  up to  $850^\circ\text{C}$  was done to burn away all the graphene. Due to the slight mass increase of silicon oxidation, there is still some error and hence this still gives a close estimate.

Specifically, in this work TGA was used to determine the weight % of carbon (graphene) in the silicon nanowire/graphene composite.

### 3.1.6 Electrode preparation technique

The electrode preparation step is a critical step required before the SiNW-G material can be tested inside a Lithium-ion cell. The SiNW-G powder must be uniformly coated and remain intact and stable on a current collector for electron transport to occur reversibly. The standard anode current collector used in industry is copper foil due to its excellent conductivity, relatively low cost, and its stability at low voltage without reacting with Li ions. The figure below shows a uniform coating or “cast” of SiNW-G material with 20wt% NaCMC and 20wt% Carbon Super P on copper foil.

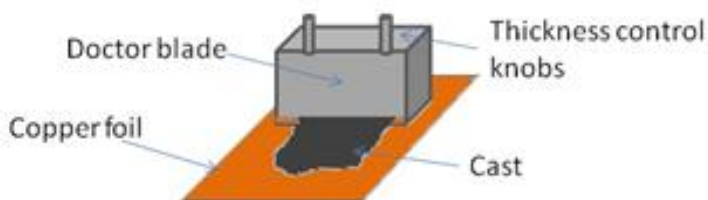


**Figure 10: SiNW-G material casted on copper foil with doctor blade**

The method of electrode preparation can greatly affect the performance of the material. There are three areas of electrode design that are studied in this section: 1) the Si/Graphene ratio in the

electrode can affect the capacity and stability of the material with a high Si amount expected to give higher capacity but lower stability, and lower Si amount expected to give lower capacity but higher stability. (2) The effect of carbon coating will also be investigated. (3) The type of polymer binder used can influence the overall structural stability and conductivity of the material.

### 3.1.7 Coin cell assembly

For electrochemical testing, the same conditions will be applied for all the batches studied. A coin cell is assembled with a metallic lithium cathode, Celgard polypropylene separator and 1 M  $\text{LiPF}_6$  in 6:3:1 (by weight) EC:DMC:FEC organic solvent as the electrolyte. EC and DMC are standard electrolyte solvents used in industry. FEC was used because it was found to stabilize the SEI layer on Si surfaces.<sup>56</sup> These components are assembled inside an Argon-filled glove box with  $\text{O}_2$  and  $\text{H}_2\text{O}$  levels  $< 0.5$  ppm to ensure no humidity can reach inside the cell and cause side reactions and short-circuiting. After the parts are assembled as illustrated in Figure 12 below, the cell is sealed using a crimper. The coin cell size is 20mm diameter and 3.2 mm thickness (coded as 2032) in the figure shown below.

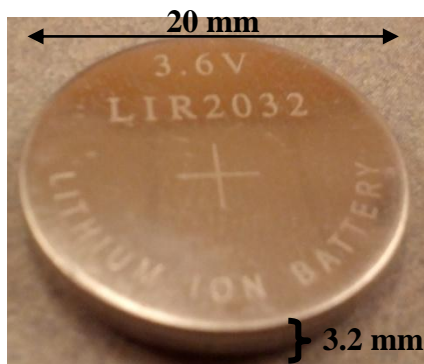
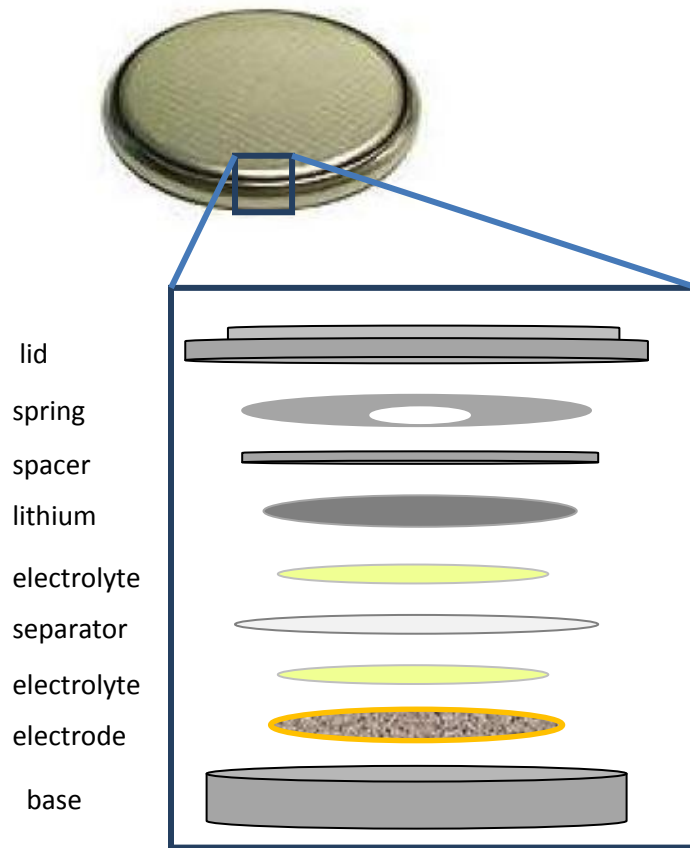


Figure 11: Coin cell dimensions



**Figure 12: Illustration of coin cell components. (Coin cell size is 2 cm wide and 3.2 mm thick)**

### 3.1.8 Battery cycler

The assembled coin cell is tested with a cycler which can test the battery with charge/discharge cycles. The desired current values, voltage limits (typically 0.01-2V for SiNW-G) and testing conditions are input in the software. For discharge, the cycler applies current and monitors and records the voltage (in mV) and capacity (in mAh) every time interval (typically 60 s) until the low voltage limit is reached (typically 0.05 - 0.01 V). For charge, the cycler draws reverse current and likewise monitors and records the data every time interval until the upper voltage limit is reached (typically 1.5 V - 2 V). The voltage vs capacity curves can be plotted based on

this time-interval data. Capacity vs cycle plots can also be extracted from the software based on the “cycle data” which gives the total capacity (in mAh) per discharge/charge cycle.

The current calculated is based on the active material mass. All cells are first cycled at the lowest current value of 0.1 A/g to see the maximum reversible capacity the active material before testing the rate capability or stability at higher current. For example, if the active material on the electrode weighs 0.5 mg (which is a typical value), then the current value set in the cycler to get 0.1 A/g would be 0.05 mA.

The Specific Capacity, in mAh/g, is also calculated based on the active material mass. The cycler results give capacity values in mAh which is divided by the mass in grams (in this case it would be 0.005 g) to obtain the Specific Capacity values in mAh g<sup>-1</sup>.

### **3.1.9 Cyclic Voltammetry**

Cyclic Voltammetry (CV), also known as linear sweep voltammetry, differs from the battery cycler in that the current is not constant. Linearly changing voltage is applied to the cell which discharges the cell to a pre-set low voltage limit (0.01V) and charges it to a pre-set high voltage limit (2 V) while measuring and recording the output current.<sup>57</sup> CV curves can reveal more information about the electrochemical behavior of the material and can be compared with fingerprint curves reported in literature. For this project, the most significant behavior would be that of silicon. Furthermore, CV is very important for the first couple of cycles because it reveals

the difference in patterns after activation of material with lithium and, in this case, the conversion of crystalline silicon to amorphous silicon.

Specifically, in this work CV was used to reveal the lithiation and delithiation of silicon at the different voltage ranges as reported in literature.<sup>55</sup> This was used to further confirm that silicon is the dominant active material in the voltage range used.

### 3.1.10 Electrochemical Impedance Spectroscopy

Electrochemical Impedance Spectroscopy (EIS) is a technique used to study the resistance and capacitance inside the cell. An equivalent circuit can be modelled for the lithium-ion cell (Figure 13) with components described as follows. Resistance associated with electrolyte solution ( $R_s$ ), charge transfer ( $R_{ct}$ ), and diffusion (Warburg diffusion resistance,  $W$ ) can all be determined and modelled. Capacitance associated with electrolyte double layer ( $C_{dl}$ ) and Solid Electrolyte Interphase (SEI) film ( $C_{SEI}$ ) can also be determined.

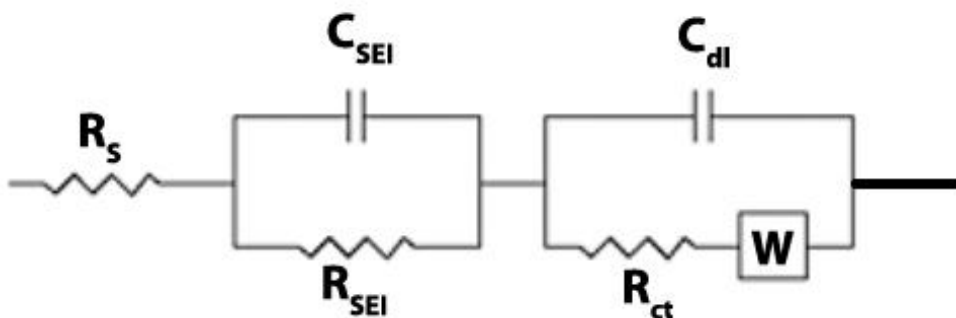
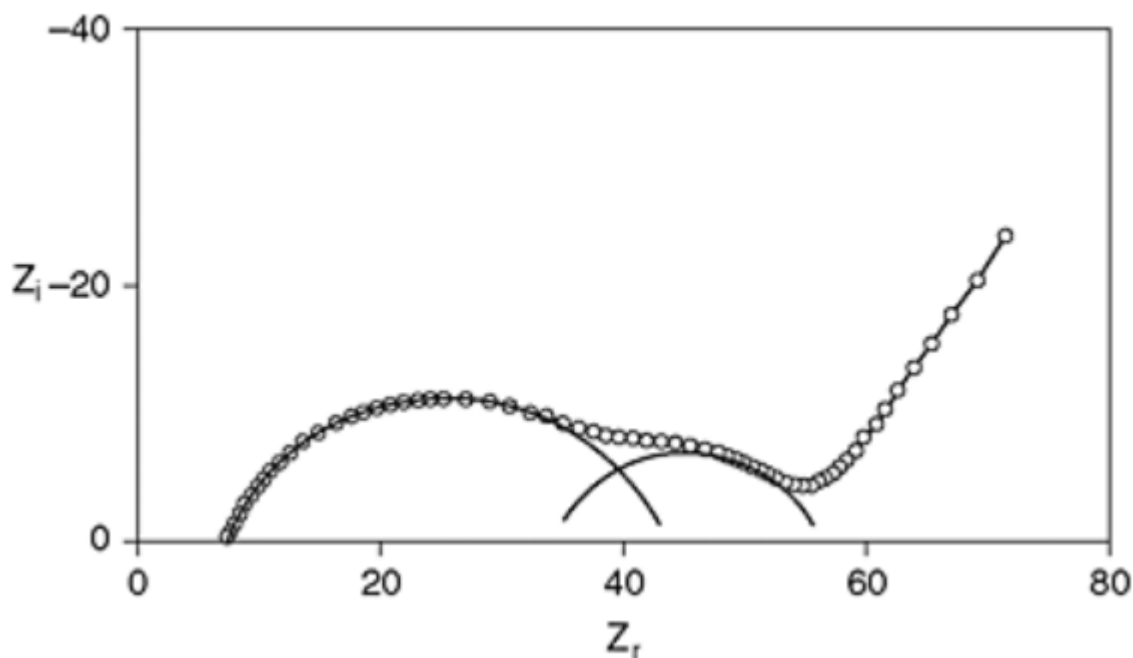


Figure 13: Equivalent circuit for a Lithium-ion cell with SEI formation (adapted from Reddy et al.<sup>57</sup>)



**Figure 14: Example Nyquist plot corresponding to the equivalent circuit in Figure 13** <sup>57</sup>

This technique works by applying a small AC signal with pre-set amplitude value (typically 5-10 mV) on the cell.<sup>57</sup> The impedance,  $Z$ , of that signal can be calculated over a frequency range (in this project 0.1 Hz to 100 kHz was used) and the resulting curve plotted by the real and imaginary component of impedance (as shown in Figure 14), called a Nyquist plot, can reflect the resistive and capacitive components of the cell, respectively. This technique is useful when comparing cells with different electrode structures to determine which has the least resistance and superior 3D conductivity. It is also useful to measure the EIS curve at different cycles of the same cell to observe the changes in internal resistance of the battery with number of cycles.

Specifically, in this work EIS was used to prove that the internal resistance of the battery is lowest with the silicon nanowire / graphene composite compared to only silicon nanowires.

### 3.2 Structural and chemical characterization of optimal batch

The optimal batch was done after investigating the effect of silicon-graphene ratio, carbon coating and changing the polymer binder on capacity and stability (please see studies in section 4). The optimal batch was found with ~50wt% graphene, carbon coated silicon nanowires and using pyrolyzed polyacrylonitrile (PPAN) binder to enhance the 3D conductivity of the electrode, as illustrated in the figure below.

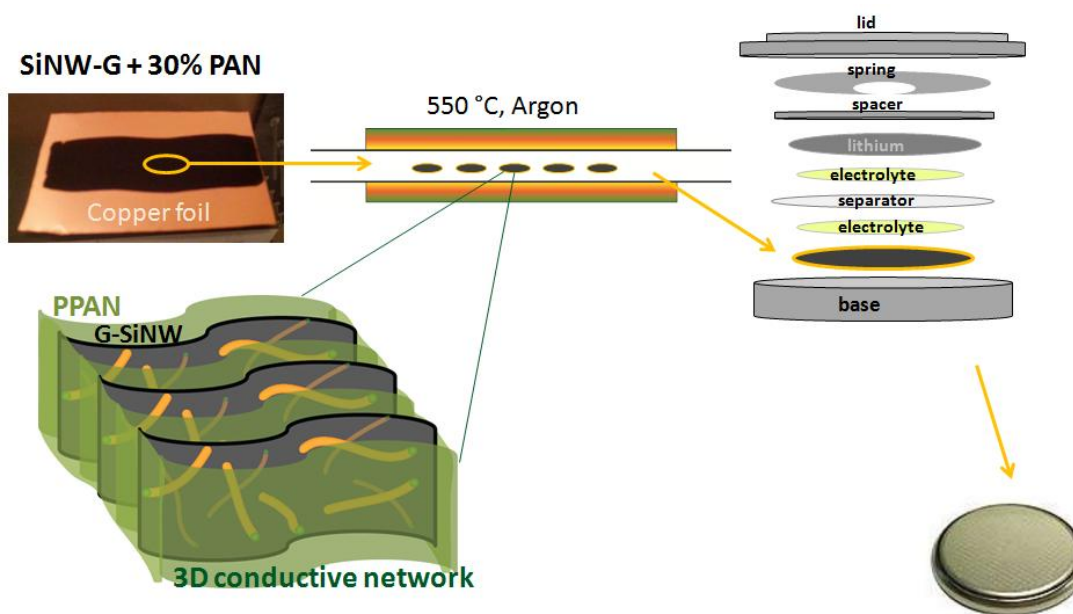


Figure 15: Illustration of optimal batch of carbon coated SiNW-G with PPAN to enhance 3D conductivity of the electrode

The following sections show the material characterization of this batch. More detailed discussion on the electrochemical characterization is found in section 4.3 and 4.4.

#### 3.2.1 Morphology Characterization

Scanning Electron Microscopy (SEM) and Transmission Electron Microscopy (TEM) were done to show the morphology of the material and the nanostructure. Figure 16 shows an SEM image

of Ni NPs on graphene which reveal 30 to 90 nm particle sizes, with most particles closer to 30-50 nm size range, which is reinforced with a larger area SEM image shown in Figure 17 (a).

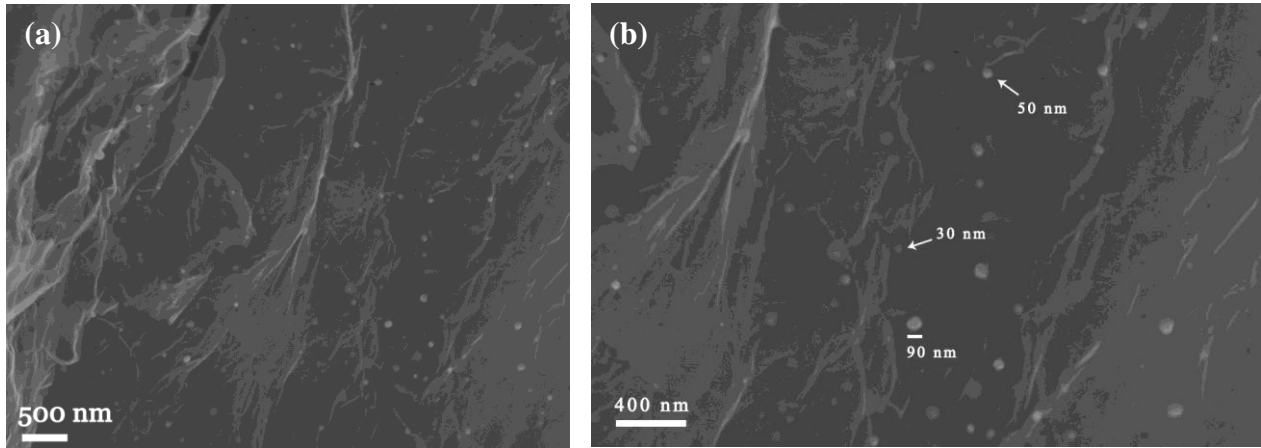


**Figure 16: (a) SEM image of NiNPs on graphene and (b) Higher resolution SEM of NiNPs on Graphene**

According to both VLS and VSS mechanisms, the Si NW diameter should be controlled by the seed diameter which is exactly what is observed with SiNM diameters in the 30 to 90 nm diameter range but mostly 30-50 nm sizes as shown in Figure 17 a-c). Furthermore, the images show that SiNWs were very well bound to the graphene nanosheets and not agglomerated together. It's important to note that the TEM sample was prepared through ultrasonic dispersion in ethanol yet the SiNWs remain intact with the graphene nanosheets indicating strong binding and no less of electrical contact through material processing.

High resolution TEM further revealed crystalline silicon nanowires and a very thin amorphous carbon coating layer as shown in Figure 17 d).

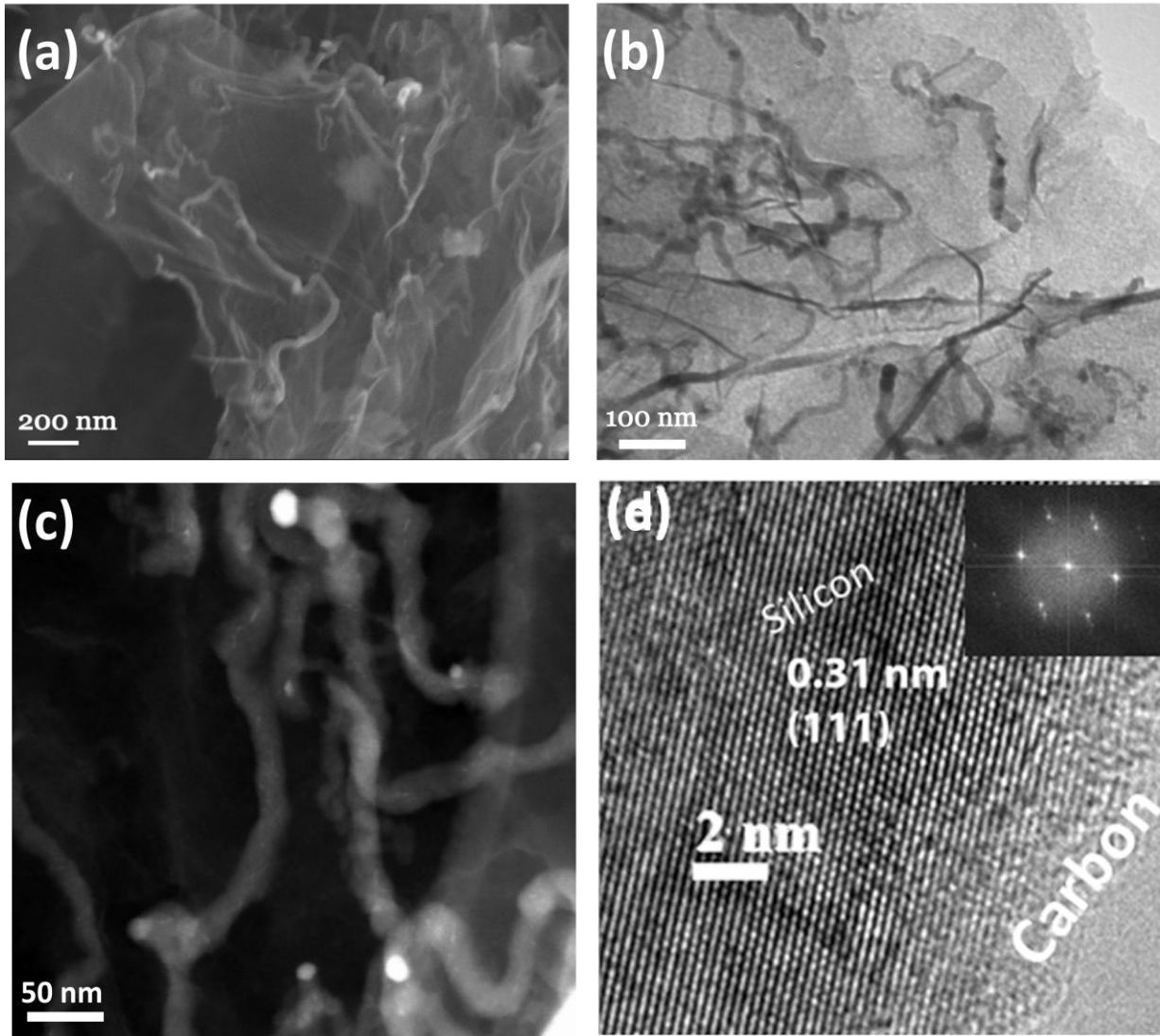


**Figure 17: a) SiNW grown on graphene (SiNW-G), b) TEM image of SiNW-G, c) HAADF-TEM (High-Angle Annular Dark-Field) of SiNW-G, and d) High Resolution TEM (HRTEM) of C-coated SiNW and the inset is the FFT diffraction pattern**

### 3.2.2 Chemical identification

Chemical identification was done using EDS elemental mapping, X-Ray Diffraction (XRD) and Raman spectroscopy.

EDS elemental mapping was done on the HAADF-TEM image as shown in Figure 18. It clearly shows SiNWs covered and supported by carbon, and Ni concentrated at the tip of the wire

reinforcing the Ni-seeded mechanism of growth. The small amount of oxygen that is not concentrated on the wires points to that the lack of oxidation of SiNWs which can be due to the protective carbon layer and the erosion of any oxides by the HCl by-product of  $\text{SiCl}_4$  reduction.

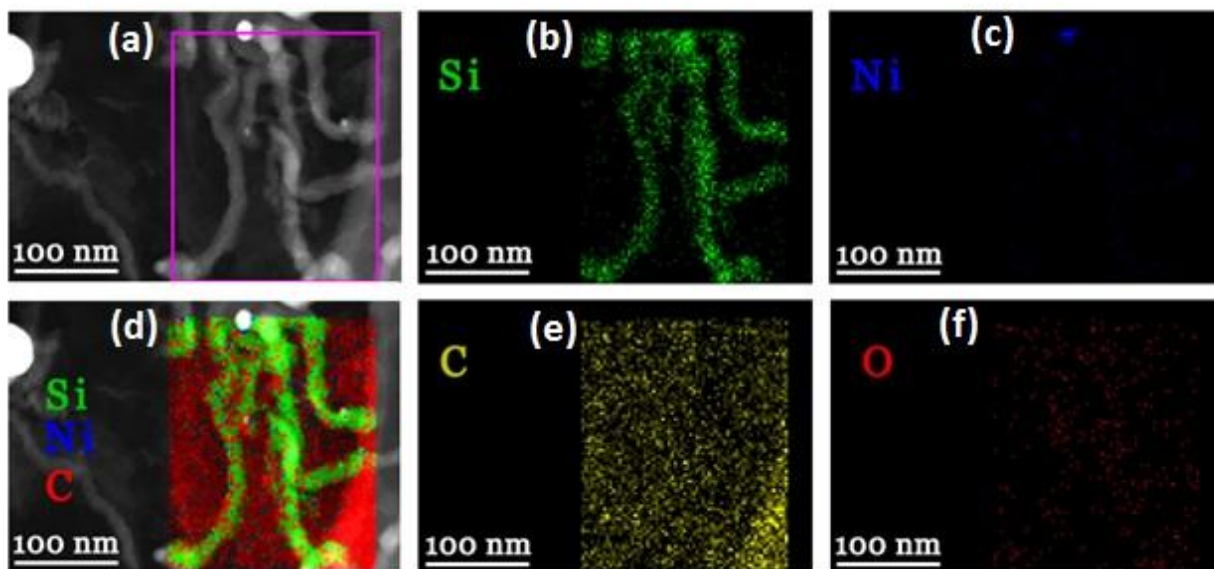


**Figure 18:** (a) HAADF-TEM of SiNW-G with EDX elemental mapping of the elements (b) Si, (c) Ni, (e) C, and (f) O and all elements in (d).

X-Ray Diffraction (XRD) of the G-NiNPs shown in Figure 19 (b) clearly showed characteristic Ni peaks at  $2\theta$  values  $25.3^\circ$ ,  $36.0^\circ$ , and  $44.5^\circ$  for the 100, 111 and 200 planes, respectively. A stronger and broader graphene peak was also shown at  $\sim 24^\circ$  for the 002 plane. This can indicate that the Ni is not completely covering the graphene otherwise the Ni peaks would be stronger and the graphene peak would be weaker.

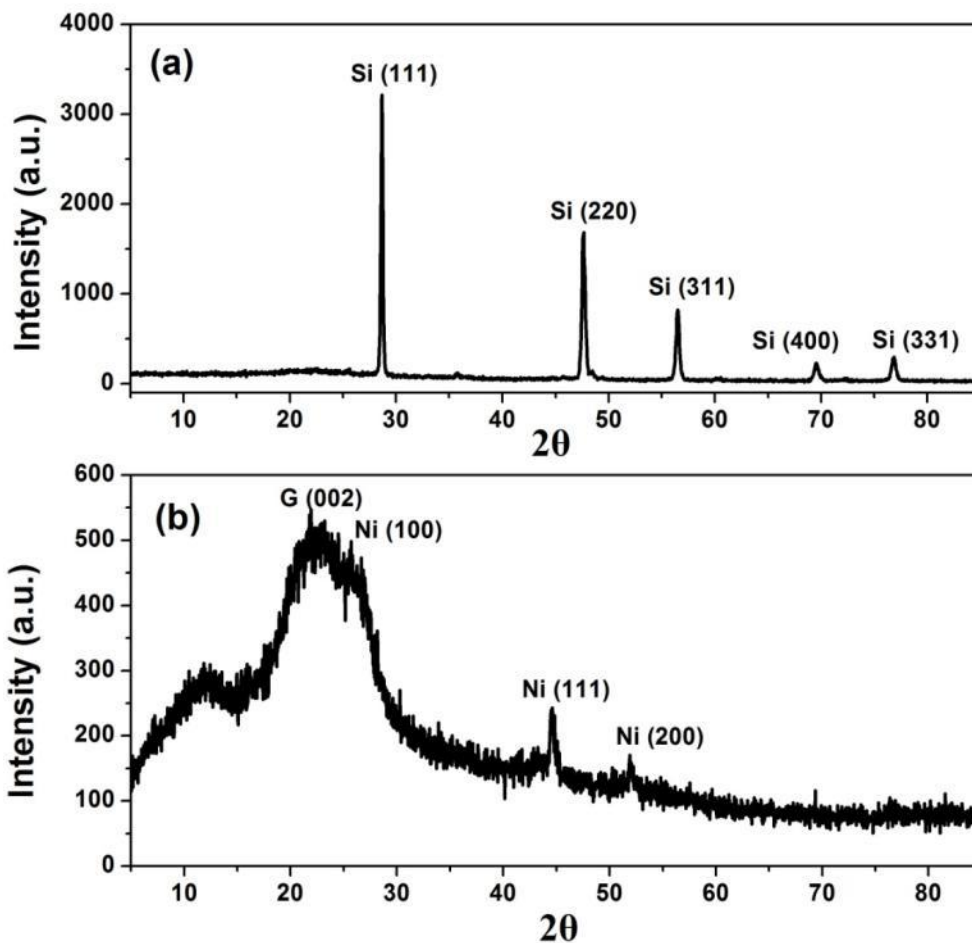


Figure 19 (a) XRD of SiNW-G and (b) NiNPs-G

XRD for the sample after Si deposition, shown in Figure 19 (a), clearly reveals all the characteristic Si peaks at  $28.4^\circ$ ,  $47.3^\circ$ ,  $56.1^\circ$ ,  $69.1^\circ$ , and  $76.4^\circ$  for the planes 111, 220, 311, 400 and 331, respectively. The graphene and nickel peaks disappear as the graphene becomes covered by Si. The Ni NPs are expected to convert to Nickel silicide as per the VSS mechanism described in section 2.2.2, but the peaks for Nickel silicide are not present due to the very small amount compared to the Si material.

Raman spectroscopy is useful not only for material identification but more importantly to reveal more features of graphene and carbon coating. The peak at  $520\text{ cm}^{-1}$  in Figure 20 (a) belongs to silicon and it shifts to  $500\text{ cm}^{-1}$  after carbon coating with Toluene as shown in (b). The decrease in the peak wave number means that there are external stresses on the Si crystal lattice, which indicates successful formation of a layer of amorphous carbon around the Si.

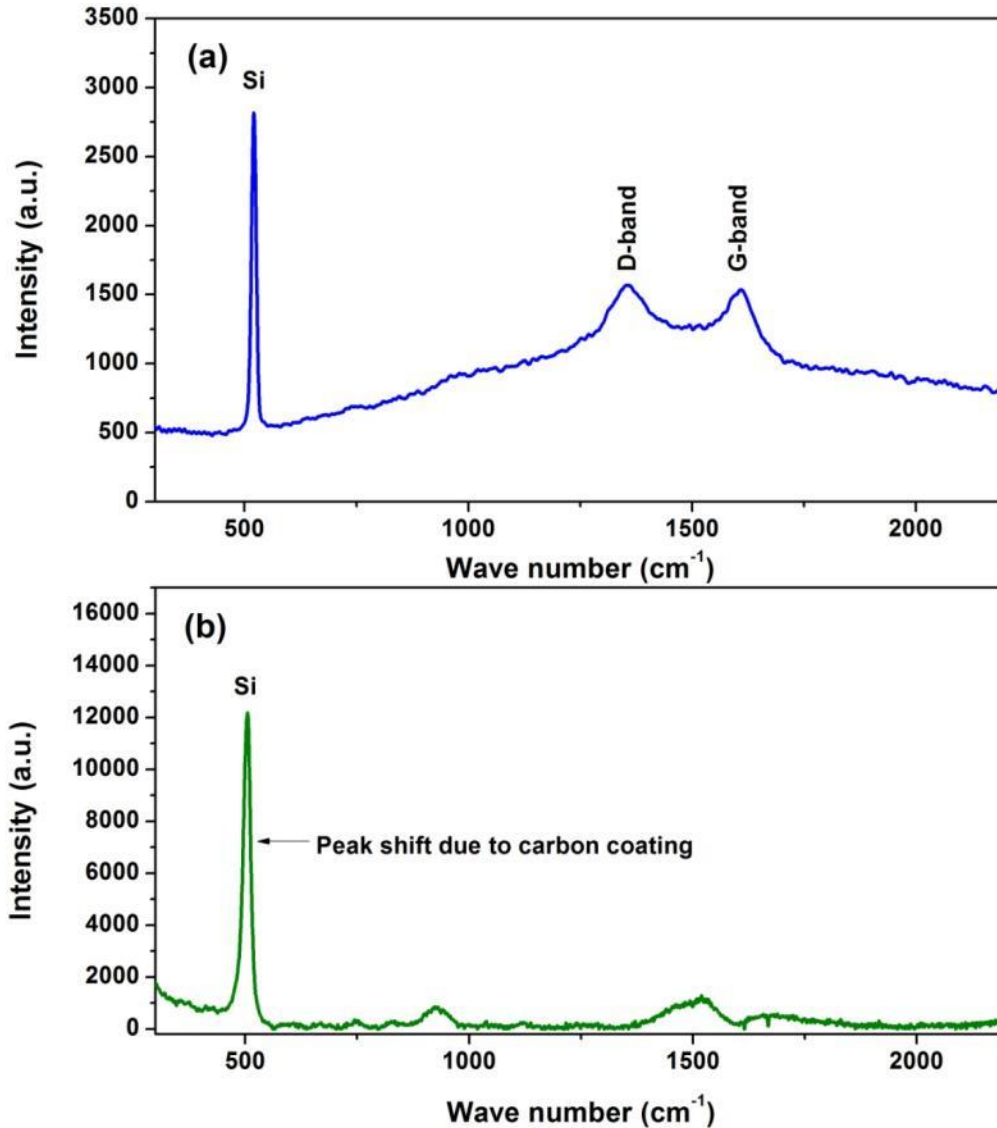


Figure 20: Raman spectroscopy of (a) SiNW on graphene and (b) Carbon-coated SiNW on graphene

The characteristic graphene peaks are at  $1357.6\text{ cm}^{-1}$  and  $1611\text{ cm}^{-1}$ , known as D and G-bands in literature. The presence of the D band correlate with the presence of defects such as edges, dislocations, cracks or vacancies in graphitic materials, which are characteristic of graphene.<sup>58</sup>

This reveals

### 3.2.3 Mass ratio determination - TGA

TGA was done to determine the ratio of graphene in the sample, shown in the figure below. This result shows a mass drop to 51% which can be estimated to 50 wt% due to the slight mass increase of silicon oxidation that starts around  $750^{\circ}\text{C}$ .

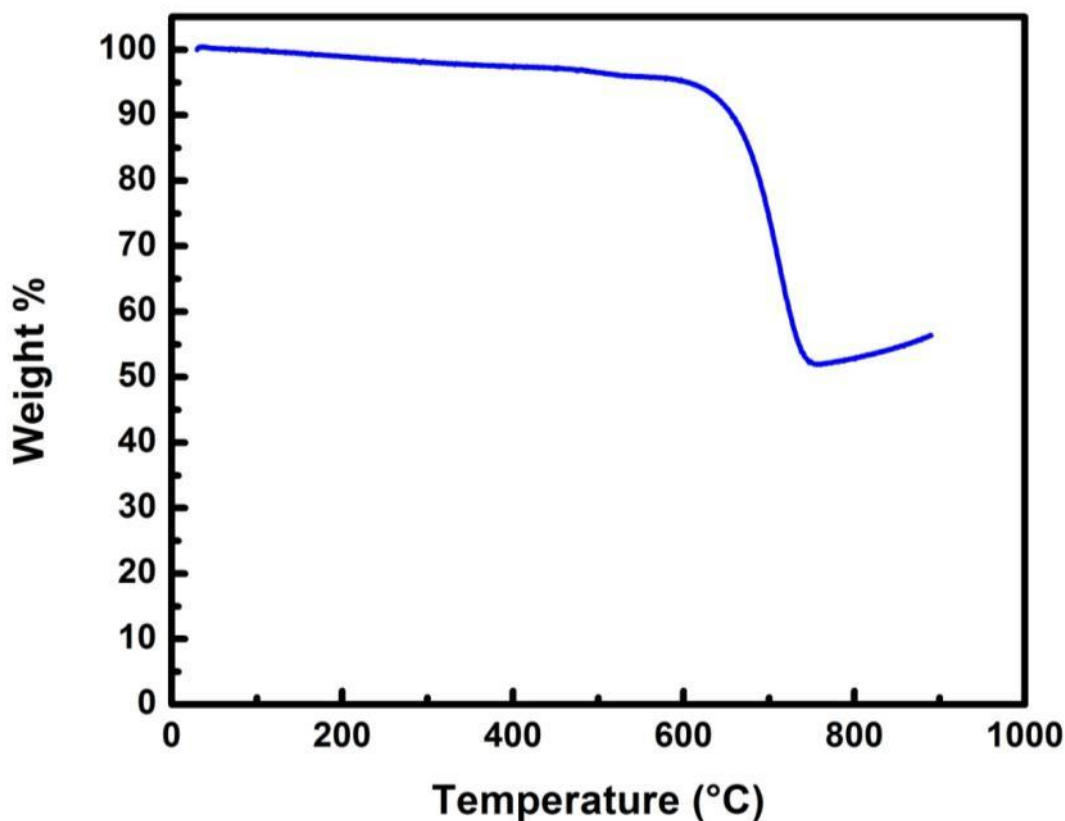


Figure 21: TGA of SiNW-G

## **4. Electrode fabrication and testing**

### **4.1 Effect of increasing Si NW content**

#### **4.1.1 Purpose of study**

The first parameter to control is the Si content. The purpose of this study is to find an optimal amount of Si for good stability yet reasonable capacity. It is expected that the higher the Si mass the higher capacity of the material but the lower the stability. The lower the Si content, the higher the stability of the material but the lower the capacity.

Furthermore, the study was done without carbon coating with toluene to see the optimal performance that can be achieved with just SiNWs on graphene by only controlling the Si/Graphene ratio.

#### **4.1.2 Experimental**

The amount of Si mass grown on graphene is simply controlled by the amount of  $\text{SiCl}_4$  used in the injection. No carbon coating step with toluene was used as that will be investigated in section 4.3.

The electrode was prepared by mixing the SiNW-G active material with 20 wt% Carbon Super P and 20 wt% NaCMC and then casting the slurry on copper foil using doctor blade followed by vacuum oven drying for 12 h at 100 °C. Disc shaped electrodes were punched from that cast and weighed. Blank copper foil discs were also weighed. The mass of the SiNW-G active material was determined by subtracting the copper foil weight from the electrode weight and factoring out the added 40% binder and Carbon Super P weight.

### 4.1.3 Results and discussion

#### *Low silicon content*

##### Morphology

The SEM image in Figure 22 reveal SiNWs with an average diameter of 40 nm that are not agglomerated together and containing voids between them for later stress relaxation. Some wires are grown horizontally along the surface of graphene and many others are grown away suspended from the graphene surface.

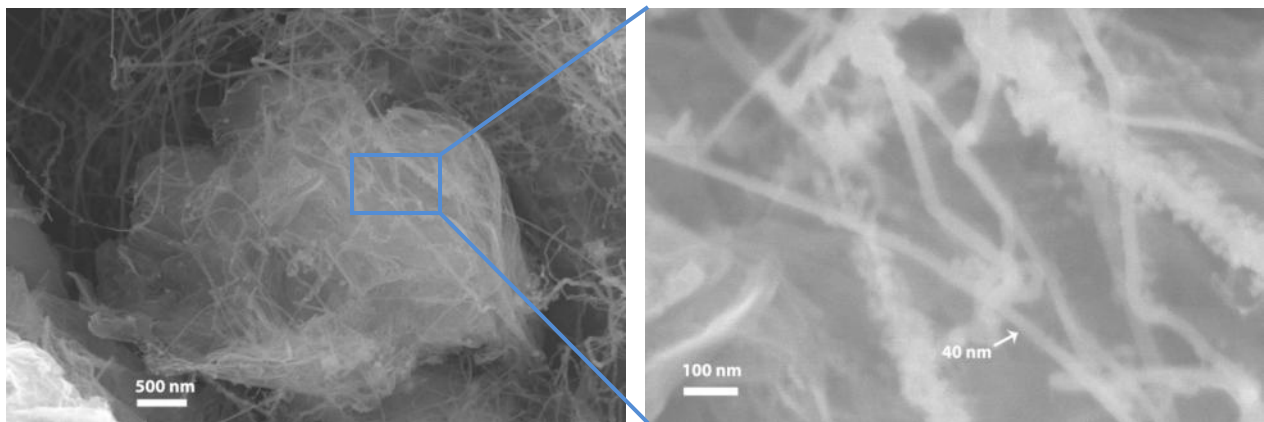


**Figure 22: SEM images of low loading SiNW-G**

The Si NWs are not completely covering the graphene with a clearly visible graphene sheets.

## Electrochemical testing

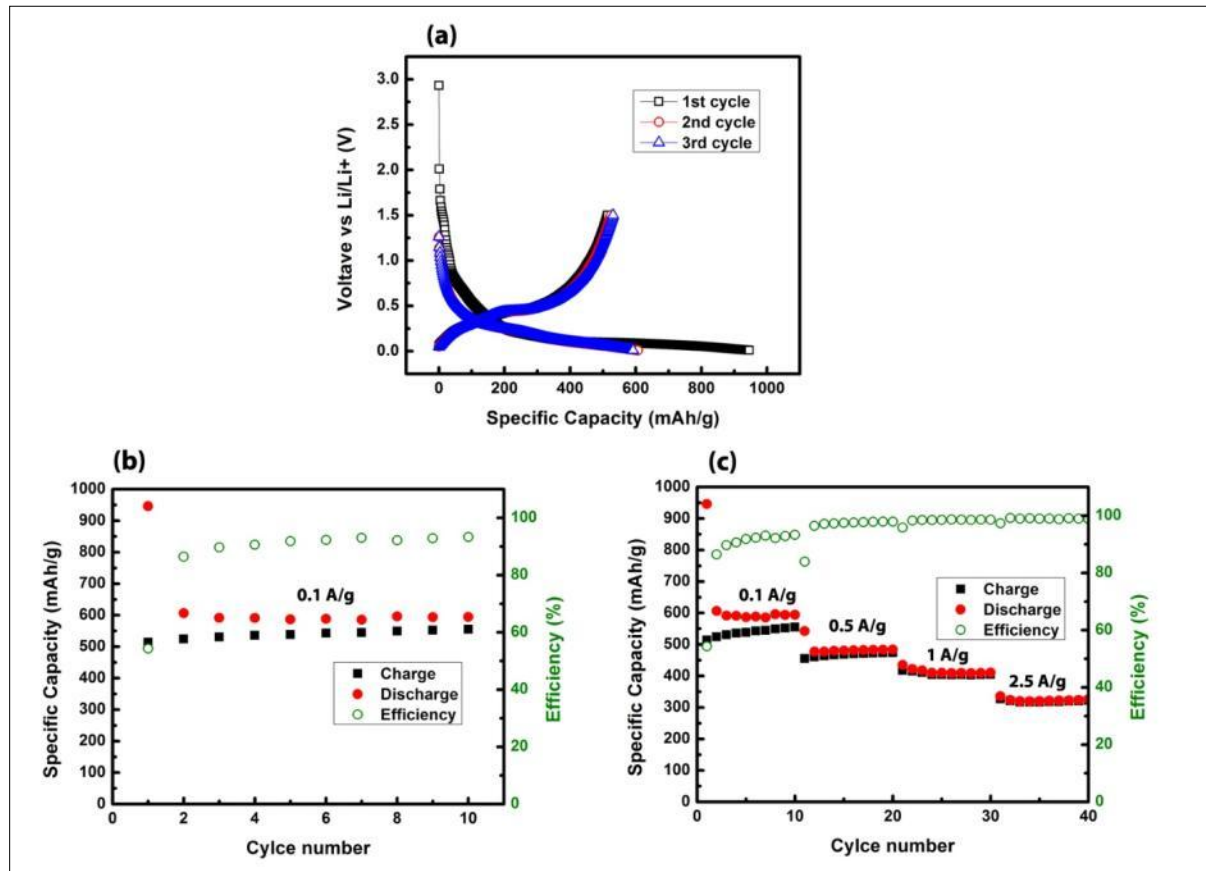


Figure 23: Electrochemical data of non-carbon coated SiNW-G with NaCMC binder, low Si content batch. (a) Voltage profile (b) Low rate (0.1 A/g) cycling (c) rate capability.

The electrochemical testing results show highly stable capacity at 550 mAh/g capacity which remains stable after several cycles. The capacity is higher than the commercial graphite capacity and the graphene theoretical at this voltage range of 0.01-1.5 V is expected to be close to the graphite (350 mAh/g). The voltage profile clearly shows the Si behavior with a plateau around 0.5 V during charging. The charge profile close to 1.5 V reveals the influence of the graphene in the electrochemical delithiation since the profile for pure Si is much steeper.

Even though the capacity is very stable, it is too low for this material to be competitive compared with literature studies of Si-based composites. A capacity above 1000 mAh/g for low rate is desired for this material to be comparable with literature studies of stable Si-based material, which is investigated in the next section.

The high stability upon increasing the current shows the role of graphene for good rate capability, but the capacity is still too low.

One other drawback of using high ratio of graphene is the poor first cycle efficiency, which is only 55% for this material. The negative effect of this is realized more critically when a full cell with limited source of Li-ions, such as  $\text{LiCoO}_2$ , as opposed to the unlimited supply of Li-ions from metallic lithium in the half cell. For this material to be considered for full cell applications, a 55% coulombic efficiency is too low – only 55% of Li-ions taken from a cathode would be available for reversible capacity. Graphene material is known to irreversibly trap Li ions on the first cycle first cycle coulombic efficiency as low as 30% for pure graphene.

### *High silicon content*

#### Morphology

Increasing the Si amount completely covered the graphene that it is no longer visible as shown in Figure 24. The SiNWs were the same size as before (40 nm average diameter), except they were packed together in a highly dense network.

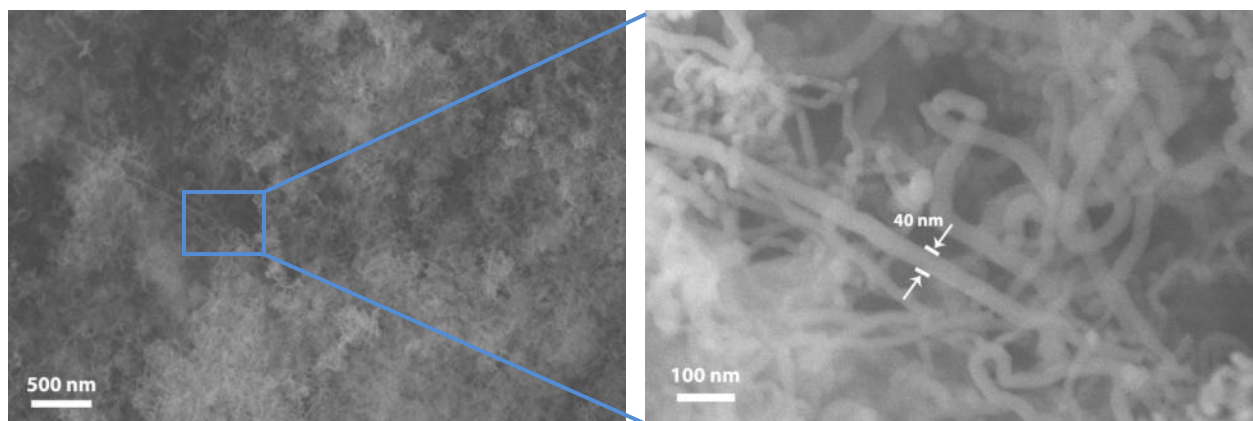


**Figure 24: Graphene completely covered with high loading of SiNW**

### Electrochemical testing

Electrochemical testing showed an increase in both the initial capacity close to 1650 mAh/g discharge and 1250 mAh/g charge and 80% first cycle efficiency, as shown in Figure 25 (a). However, the stability is very poor with rapid capacity decay to 300 mAh/g after 25 cycles. This can be attributed to the loss of electrical contact with the carbon super P additive over cycling and the low overall structural stability with little space to accommodate the volume expansion of SiNWs. The voltage profile shows a much stronger plateau around 0.4 V and a much steeper charge profile close to 1-2 V because of the dominant contribution of Si to the active material.

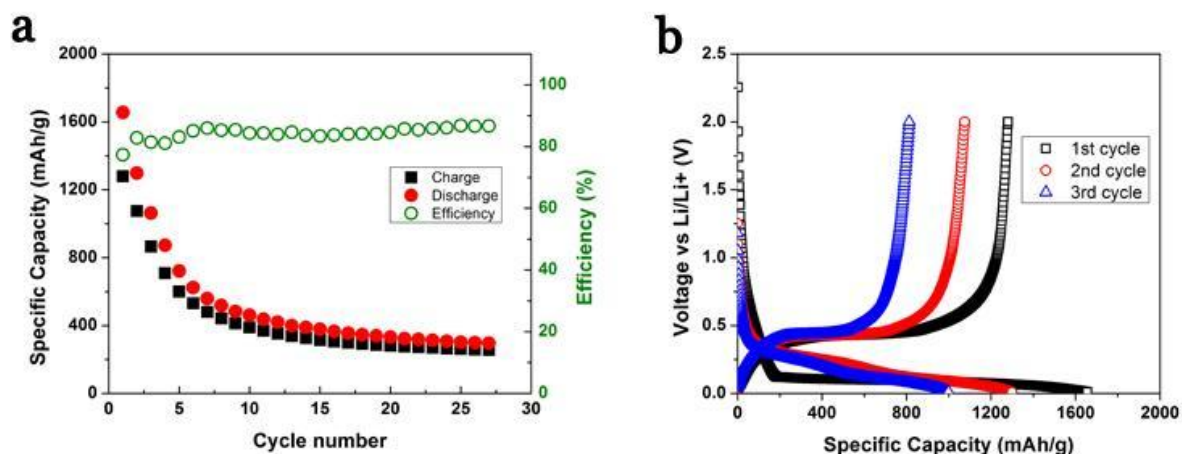


**Figure 25: (a) cycle data and (b) voltage profile of non-carbon coated high loading SiNW on G with NaCMC**

## 4.2 Effect of carbon coating

### 4.2.1 Purpose of this study

It was found that adding a high amount of Si helped increase the capacity over 1000 mAh/g and the coulombic efficiency to 80% but the capacity decay was very rapid. This section investigates the effect of adding a carbon coating step to further improve the capacity and stability of the material while keeping a reversible capacity above 1000 mAh/g.

### 4.2.2 Experimental

Carbon coating was done by injecting Toluene (under room temperature, no ice bath) in the CVD system (see **Error! Reference source not found.**) at 900°C under 300 sccm H<sub>2</sub> flow (reduced from 500 sccm due to the higher vapor pressure of Toluene). Typically 50 µL of toluene is injected after 300 µL of SiCl<sub>4</sub> added to 15 mg of G-NiNPs, yielding approximately 10% carbon coating in the whole SiNW-G-C material.

For electrochemical testing, the electrode was prepared with 70wt% SiNW-G-C material, 20 wt% NaCMC and 10wt% Carbon Super P and casted on copper foil with Doctor blade. The ratio of Carbon Super P was reduced because of amorphous carbon already added in the carbon coating step.

### 4.2.3 Results and discussion

#### Morphology

SEM was done to show the carbon-coated SiNWs. Figure 26 (a) shows the 40 nm NiNPs on Graphene that was used to grow the SiNWs. Figure 26 (b) shows the carbon-coated SiNW. It is

clearly evident that the diameter of the wires increased much more than previous batches and more than the size controlled by the Ni Catalyst as per the VSS mechanism.

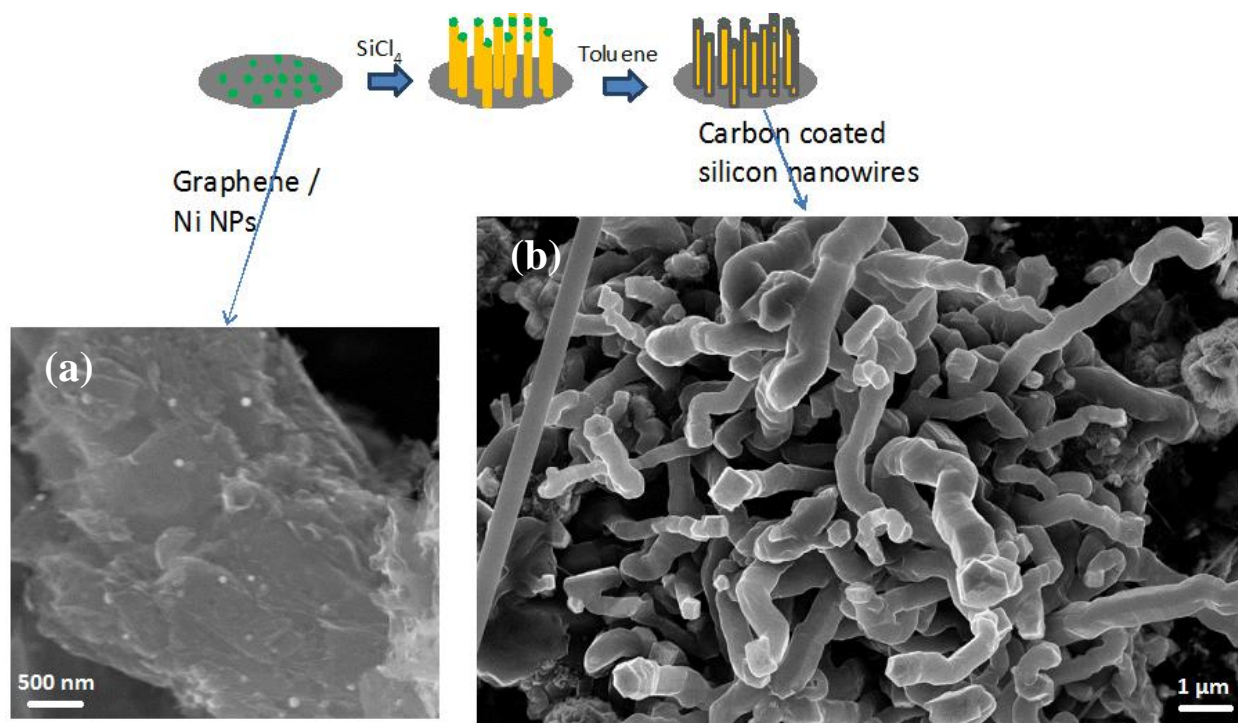


**Figure 26: SEM image of (a) G-NiNPs and (b) Carbon coated Si NWs on Graphene**

This increase in diameter points to the presence of carbon coating around the wires. Raman spectroscopy of this batch was already discussed in section 3.2, Figure 20 which showed that the Si peak was shifted from  $520\text{ cm}^{-1}$  to  $500\text{ cm}^{-1}$  due to the external stress on the Si lattice from the carbon coating.

### Electrochemical testing

Electrochemical testing showed a significant increase in the stability of the material with the capacity reaching 600 mAh/g after 20 cycles as opposed to 300 mAh/g after 20 cycles for the previous batch with the same initial discharge capacity of 1650 mAh/g. There was definitely a lower rate of decrease in capacity. Furthermore, even though a medium amount of silicon was

used (less than the high silicon loading batch in the previous section), the initial capacity was comparable, showing the role C-coating played in improving the capacity. This could be due to improved electron transport to SiNWs surfaces with no contact to graphene or carbon super P. The first cycle efficiency is 60% due to the larger ratio of graphene.

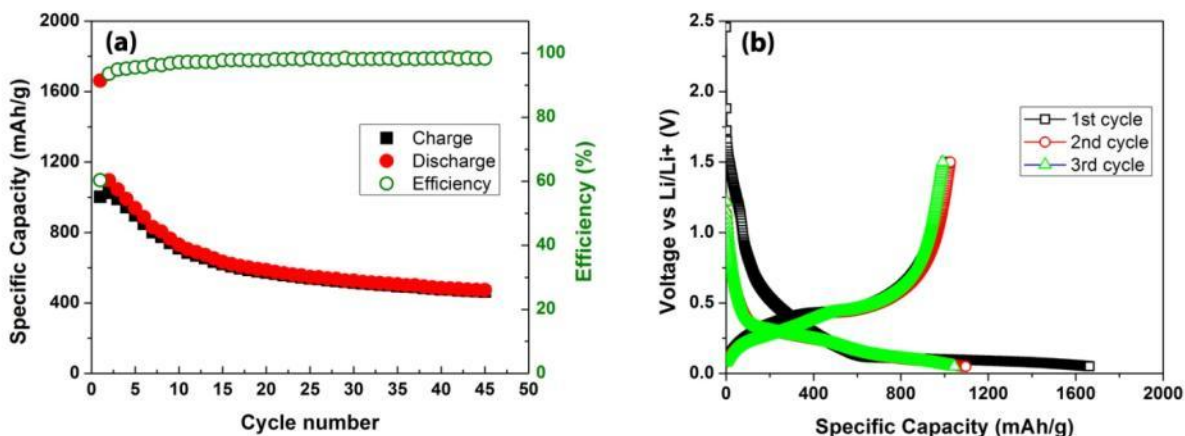


**Figure 27: (a) cycling and (b) voltage profile of C-coated SiNW with NaCMC**

Furthermore, the SEI layer formation on SiNWs can be more stable with if separated from the Si surface with a carbon layer.<sup>59, 60</sup>

However, while the stability is better than the previous batches, it is still not good enough for this material to be usable for PHEV and HEV applications that require long lifetime. A reduction of capacity below 600 mAh/g after 40 cycles is inferior to other reported graphene/silicon composites.<sup>42, 43</sup> Therefore, some improvements in electrode preparation are required to maximize the performance of this material.

In the next section, the type of binder will be investigated to further improve the capacity and stability of the material.

## **4.3 Effect of binder**

### **4.3.1 Purpose of this study**

Previous batches have shown that adjusting the silicon content and adding a carbon coating step was not enough to achieve high capacity (above 1000 mAh/g reversible) and high stability performance. The final element of electrode structure is the polymer binder. In previous batches, NaCMC has been used which only provides structural stability, but does not improve the 3D conductivity.

A self-standing, binder-free electrode will be studied as a control to see the performance without binder, but it itself is an interesting electrode structure since it removes the copper foil inactive mass which increases the actual specific capacity of the whole electrode (per mass of electrode not just active material), and also has been studied in literature for flexible battery applications.<sup>61</sup>

The second electrode structure studied would include a binder which improves the 3D conductivity of the electrode: pyrolyzed PAN (PPAN).<sup>62</sup> The inability to increase the initial capacity to above 1600 mAh/g and the reversible capacity to above 1000 mAh/g may be due to the inaccessibility of some SiNWs by Li ions due to low electrical contact between the graphene nanosheets. Graphene has great 2D conductivity, but it suffers in terms of 3D conductivity. The inclusion of PPAN which synergistically acts as a binder and conductive coating may enhance the overall performance of the battery.

## 4.3.2 Experimental

### 4.3.2.1 Preparation of Self-Standing, binder-free C-coated SiNW-G

To produce self-standing SiNW-G, the initial G-NiNPs template is developed in a way that forms a stable self-standing film without the need for a copper foil support or binder. In order to do that, an additional step is added after drying the GO-Ni(NO<sub>3</sub>)<sub>2</sub>·6H<sub>2</sub>O mixture. If the dried film that remains on the beaker is immediately removed after drying then the CVD process would result in a powder not a self-standing film, but if it is left for further heating at 90°C under the hot plate for 1 hour the film starts to become more stable and remains self-standing even after undergoing the SiCl<sub>4</sub> CVD at high temperature. This could be due to the partial reduction of GO and dehydration of Ni(NO<sub>3</sub>)<sub>2</sub>·6H<sub>2</sub>O. After SiNW growth, the film was cut into small disc-like shapes for coin cell assembly and weighed. Pictures of the films are shown below. The entire mass of the self-standing electrode was used for capacity calculation and current calculation.



Figure 28: Self-standing electrodes of C-coated SiNW-G

#### ***4.3.2.2 Preparation of C-coated SiNW-G-PPAN electrodes***

To prepare this electrode, firstly the C-coated SiNW-G material is prepared as previously described in section 3. A mixture of 70 wt% SiNW-G and 30 wt% PAN is prepared by a combination of physical and ultrasonic mixing. Ultrasonic mixing is important for the polymer to reach between the SiNW-G sheets. A thick slurry is then obtained and casted on copper foil current collector.

Electrodes were then punched and the SiNW-G mass was obtained. The electrodes were then heat treated at 550 °C for 2 hours in Argon atmosphere to partially carbonize the PAN and enhance the 3D conductivity of the electrode material. The electrode remained intact and well attached to the current collector after heat treatment.

### **4.3.3 Results and discussion**

#### ***4.3.3.1 Self-Standing, C-coated SiNW-G***

Morphology of this material is the same one as shown in Figure 26.

##### *Electrochemical performance*

The battery performance is slightly worse than the same batch with NaCMC binder showing that the NaCMC binder played some role in enhancing the performance of the material, but only slightly. The initial capacity is comparable to the batch with NaCMC binder (~1600 mAh/g) but the capacity drop is slightly sharper going all the way to down to 350 mAh/g after 45 cycles.

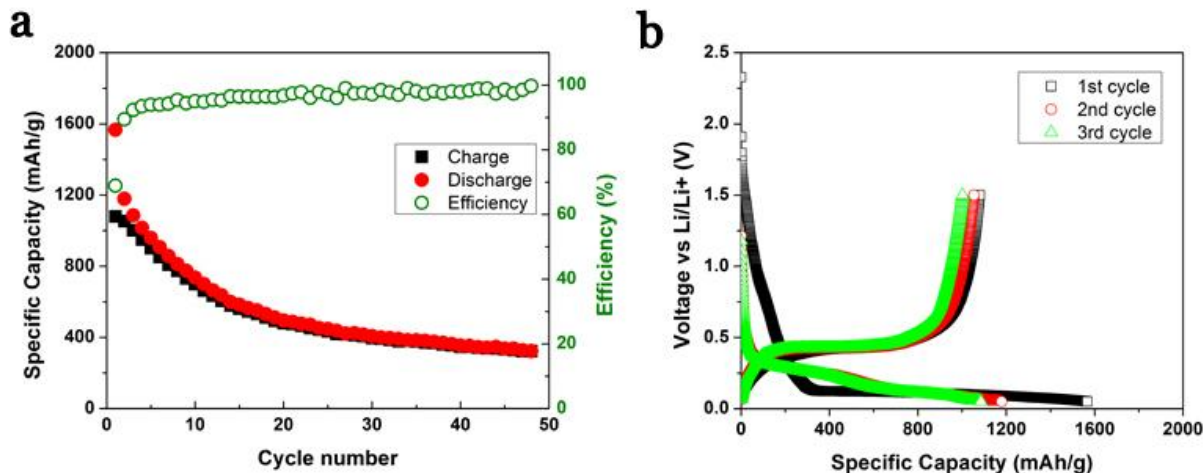


Figure 29 (a) cycling and (b) voltage profile of C-coated, self-standing SiNW-G

The same material casted with 20wt% NaCMC binder and 10wt% Carbon Super P stayed at 500 mAh/g after 45 cycles, as shown in Figure 27. The voltage profile shows similar behaviour.

#### 4.3.3.2 SiNW-G with PPAN

The morphology and structural characterization of this material was already discussed in section 3.3

##### Electrochemical performance

The electrochemical testing of this electrode structure showed a great boost in performance with much higher capacity and stability. An initial discharge and charge capacity close to 2100 mAh/g and 1500 mAh/g (respectively) and efficiency of 65% was observed as shown in Figure 30 a).

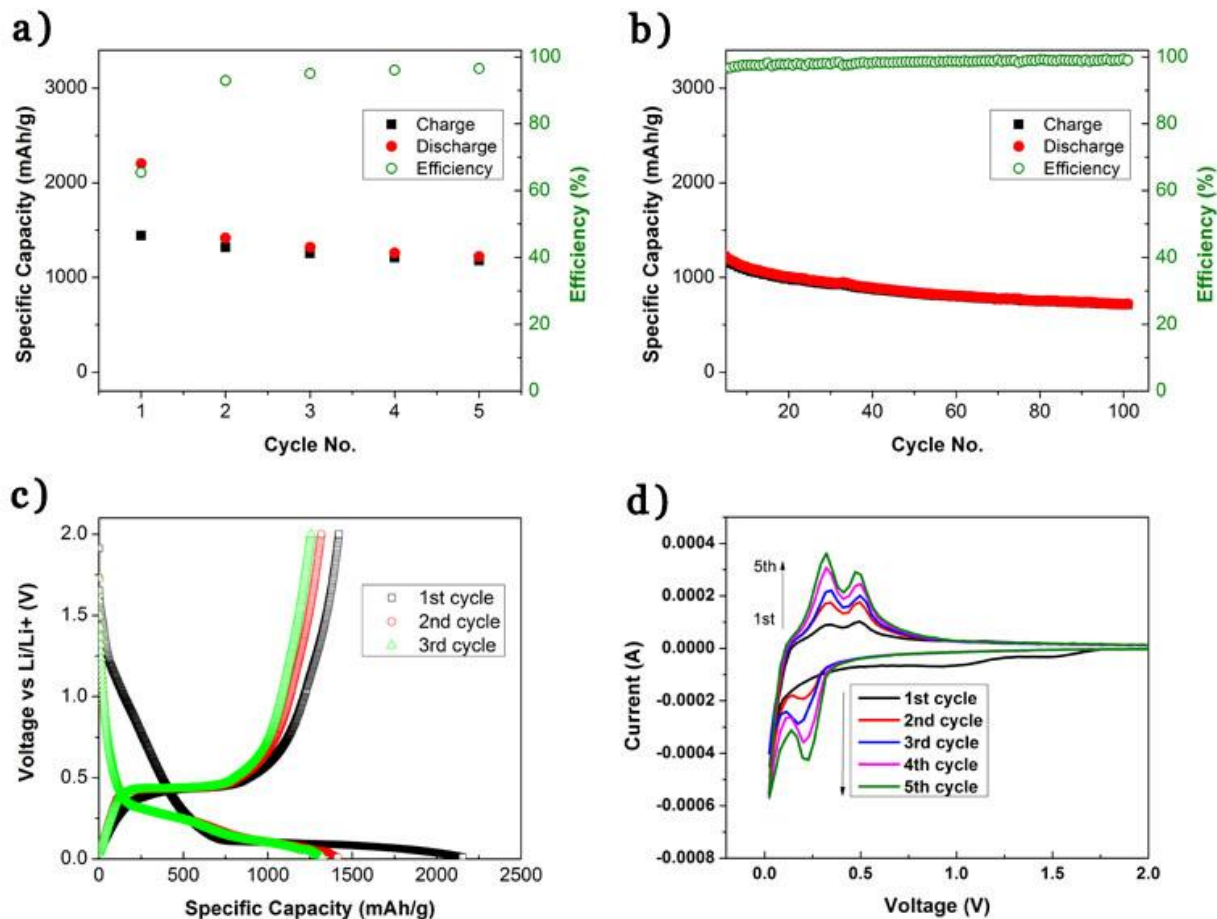


**Figure 30: Electrochemical performance of SiNW-G-PPAN showing (a) First 5 cycles at 0.1 A/g b) remaining cycles at 0.1 A/g (c) Voltage profile and (d) CV profile**

Continued cycling up at 0.1 A/g up to 100 cycles in b) show much improved stability from all other batches with 33% capacity from ~1200 mAh/g to ~800 mAh/g, corresponding to 0.33% capacity drop per cycle only. The voltage profile shows the signature silicon profile as before.

Cycling Voltammetry (CV) was done with a scan rate of  $0.05 \text{ mV s}^{-1}$  at 0.01-2 V range, as shown in Figure 30 d). The first CV cycle shows a peak starting at 0.15 V all the way to 0.01 V corresponding to the cathodic lithiation of Si to  $\text{Li}_x\text{Si}$ .<sup>63</sup> The anodic peaks at 0.32 V and 0.51 V correspond to the delithiation of  $\text{Li}_x\text{Si}$  back to Si. The subsequent cycles show an additional cathodic peak appearing at 0.20 V which becomes broader and stronger with number of cycles

together with the anodic peaks at 0.32 V and 0.51 V. This corresponds to the conversion of crystalline silicon to amorphous with the lithiation/delithiation alloying/de-alloying mechanism.

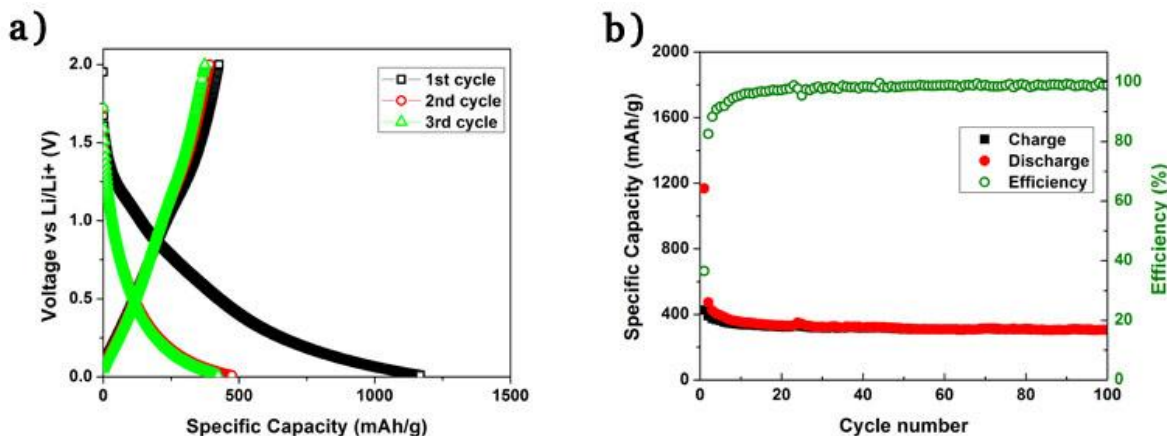


**Figure 31: (a) Voltage profile and (b) Cycle data of Graphene reference material at 0.1 A/g**

As a reference, graphene material without SiNW was also electrochemically tested in the same voltage range at 0.1 A/g showing distinctly different voltage profile features as shown in Figure 31 a). The long plateau on the first discharge and charge that are unique to silicon are not present. Cycle data in b) show a very low first cycle efficiency of 30% which is less than half of that for SiNW-G. The reversible capacity is around 380 mAh/g showing that only approximately 35% of the capacity contribution comes from graphene and the remaining comes from silicon for cycling at 0.1 A/g.

The low coulombic efficiency of graphene has been attributed to the trapping of Li ions in the defect sites of graphene in addition to the SEI layer formation on the electrode.<sup>42</sup> When lower ratio of graphene is used in the electrode, the extent of Li ion trapping in graphene defect sites decreases and hence the first cycle efficiency of the SiNW-G composite is increased to 65%.

Even lower graphene content as discussed in the first batch with high silicon loading showed 80% first cycle efficiency but without sufficient stability.

## 4.4 Further analysis of optimal batch SiNW-G-PPAN

### 4.4.1 Rate capability analysis

To test the rate capability of the material, the battery cyclers is set with incremental current values every 5 cycles for both discharge and charge as shown in Figure 32 a). The voltage profile in b) shows the typical Si values as before and the distinct Si features dominating in activity even at a very high current of 10 A/g. Long range cycling at 1.7 A/g and 6.8 A/g as shown in c) and d) respectively show good capacity and stability even at high current. This is particularly the case for the one running at 6.8 A/g with the most superior stability of all other cells. This could be due to the fact that at such high current, Li ions are only able to reach the outer shell of Si NWs leaving un-reacted Si core which may stabilize the wire morphology.

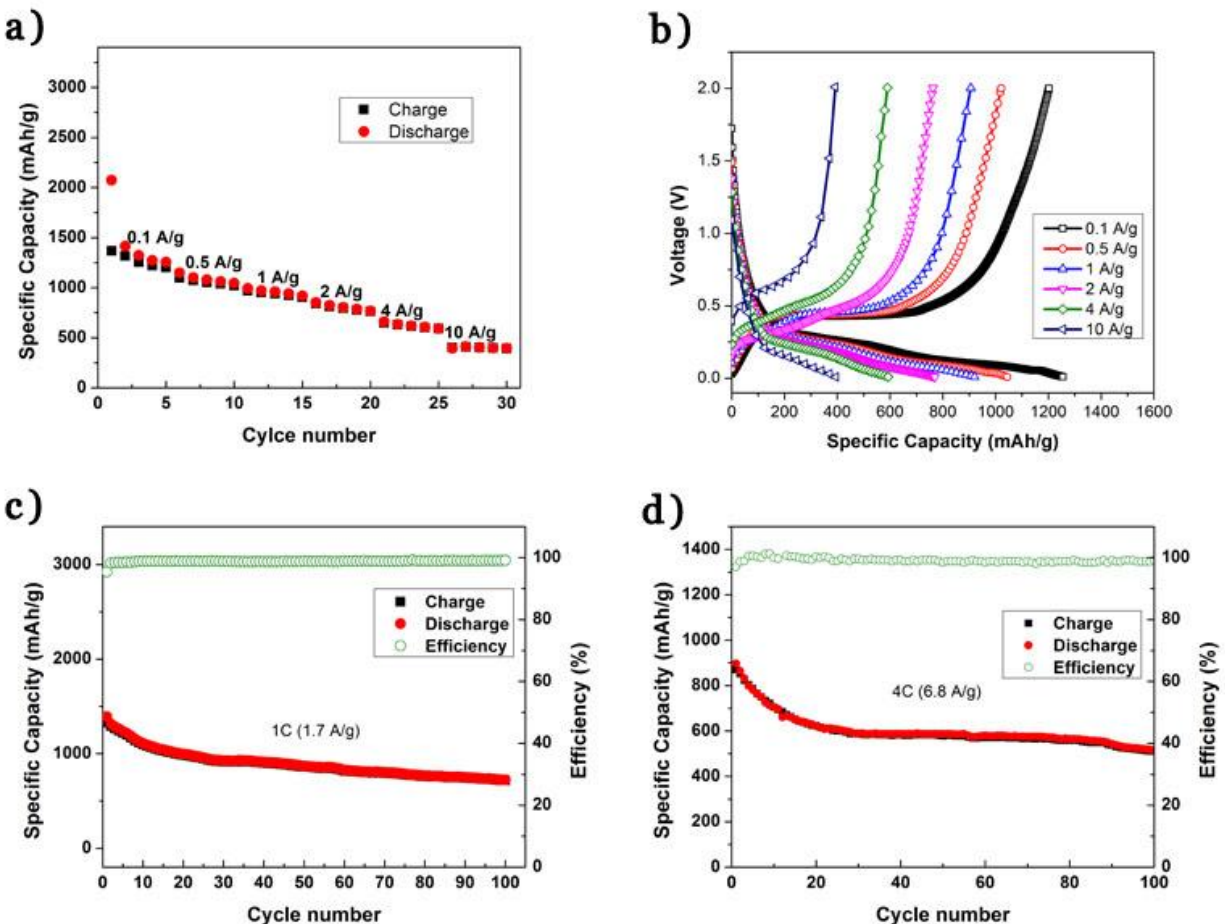


**Figure 32: SiNW-G-PPAN battery performance for (a) rate capability cycling, (b) rate capability V profiles, (c) cycling at 1.7 A/g after 5 cycles conditioning, and (d) cycling at 6.8 A/g after 5 cycles conditioning**

Figure 33 shows extended rate capability with continued cycling at 2A/g for 100 cycles compared with the graphene and unsupported SiNWs. This curve shows that at high current, the capacity of stand-alone graphene or standalone SiNWs are only a fraction of the SiNW-G composite. The rate capability data of the SiNW reference shows much larger capacity drops between each current interval. The Graphene reference shows the lowest capacity drops but also the lowest overall capacity. Overall, the SiNW-G material shows more than 3 times the capacity at high charge/discharge rate which shows the synergistic performance of SiNWs grown on Graphene.

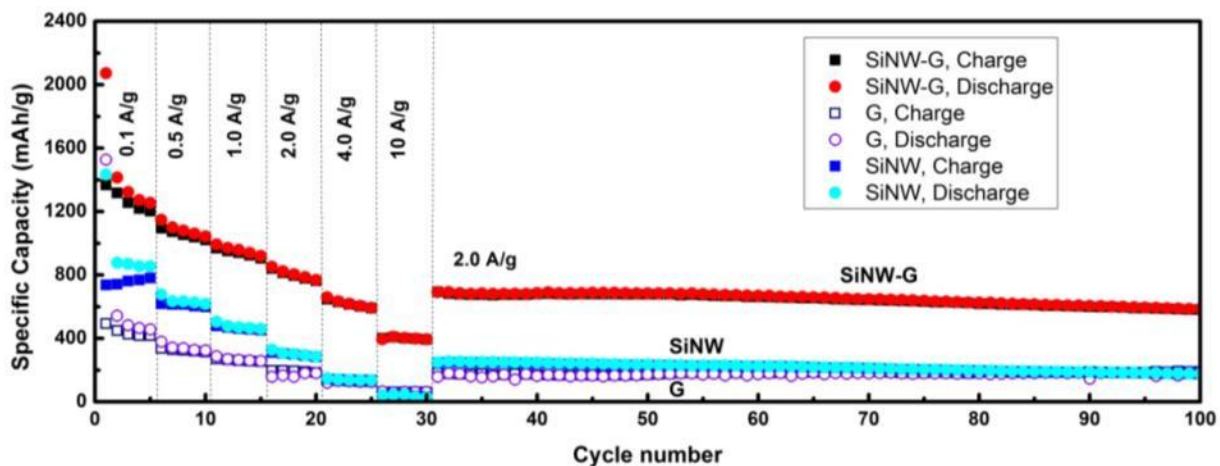


**Figure 33: Rate capability comparison with SiNW-G, SiNW without G, and G reference**

The ability to maintain higher capacity despite increasing the current shows that the fast electron mobility required at such high currents is matched with the fast electron mobility possible at the interface between silicon and graphene which is not achievable without the graphene surface.

#### 4.4.2 EIS analysis

EIS was done the SiNW-G electrode after the first discharge as shown in Figure 34 (a). This analysis is useful to see the SEI layer formation that is most significant on the first discharge. The plot looks almost identical to the Nyquist plots of the equivalent circuit model reported in literature that accounts for SEI layer formation.<sup>57</sup> Figure 34 (b) Show a comparative EIS plot after 100 cycles of SiNW-G, G ref, and SiNW ref clearly showing the superior 3D conductivity of the SiNW-G with lowest impedance values, corresponding to low resistance. It is also important to note that the impedance dropped dramatically from the first discharge to the 100<sup>th</sup> discharge indicating the role lithiation and activation of the material has in further reducing the internal resistance of the cell. This may also explain the lower impedance values for SiNW-G than G which may be due to the much higher extent of lithiation. It can also be due to the superior 3D conductivity provided by the carbon-coated SiNWs electrically linking the graphene sheets together as opposed to standalone graphene sheets.

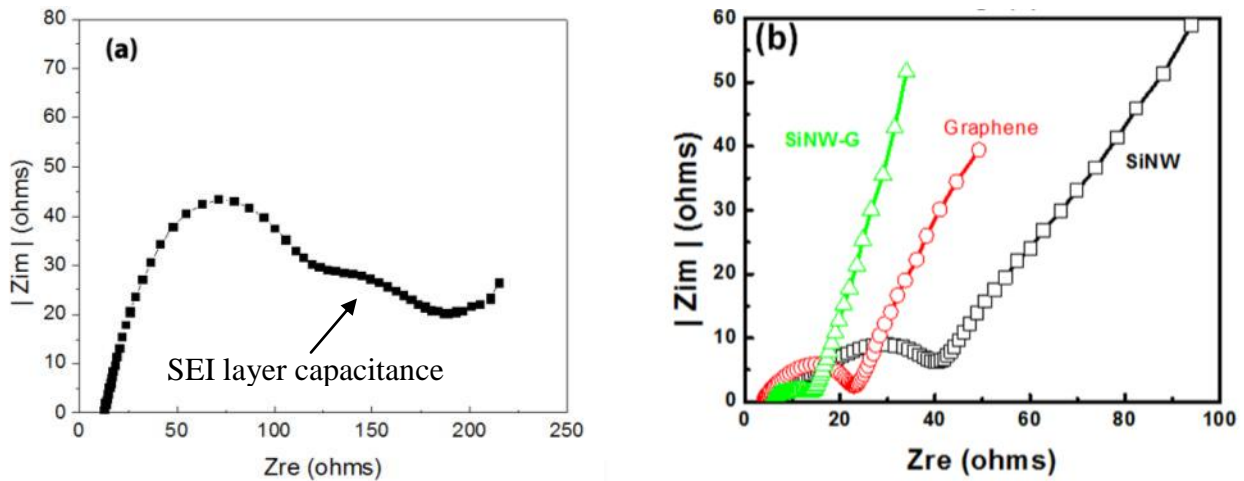
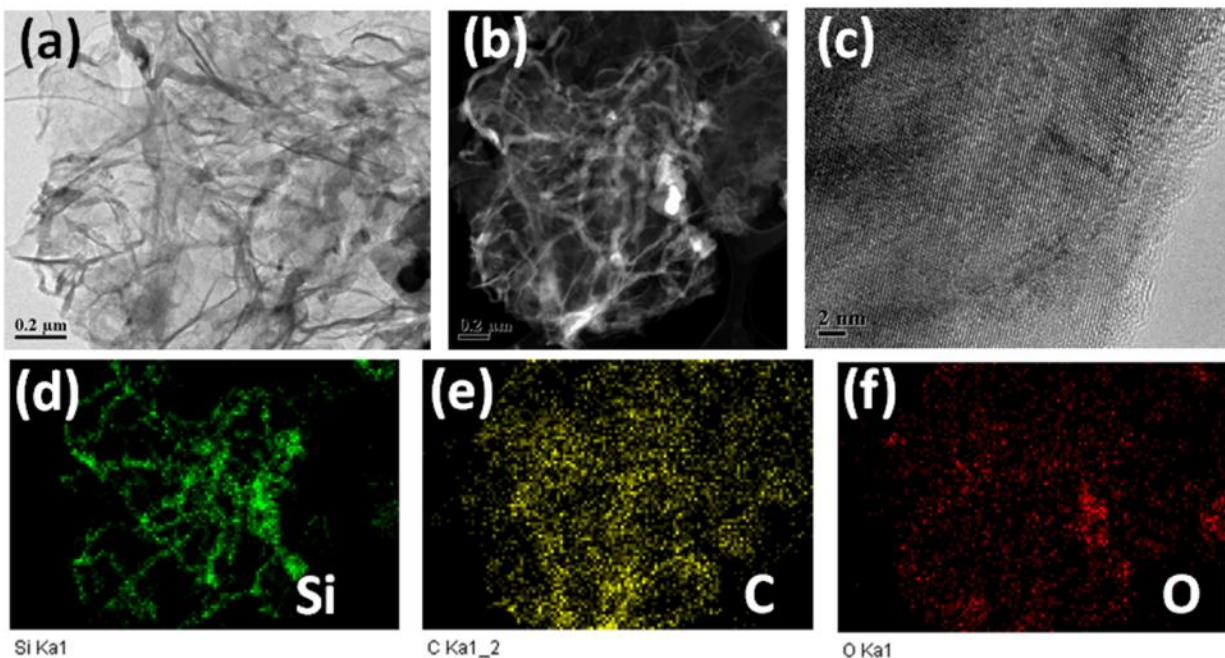


Figure 34: EIS data after (a) first discharge of SiNW-G and (b) 100th discharge for SiNW-G, SiNW and G electrodes

The charge transfer resistance in the model explained in section 3, relates to the end of the semicircle, with the lowest value around 15 ohms for SiNW-G followed by 22 ohms for graphene and 40 ohms for non-supported SiNWs. This reinforces the superior rate capability of the SiNW-G material with the lowest charge transfer resistance enabling fastest charge/discharge rates.

#### 4.4.3 TEM after testing

After 100 cycles were completed, the coin cell was carefully opened using pliers, and the cycled electrode was taken out and washed with DMC to remove any traces of electrolyte and organic solvent. A segment was cut from the electrode and dispersed in ethanol with ultrasonic bath, and the resulting material was prepared for TEM imaging.



**Figure 35 (a) TEM image, (b) HAADF-TEM image, (c) HRTEM image and EDX mapping of (d) Si (e) C and (f) O for G-SiNW electrode material after 100 discharge/charge cycles**

The TEM results show that the electrode nanostructure was maintained even after 100 cycles. Clearly, SiNW remained intact on the graphene nanosheets and surrounded by carbon material.

The increase in O content is likely from the organic deposits in the SEI layer in the form of lithium carbonate ( $\text{Li}_2\text{CO}_3$ ) and lithium alkyl carbonates ( $\text{ROCO}_2\text{Li}$ ).<sup>60</sup>

## 5. Summary and Future Work

To summarize, silicon nanowires (SiNWs) were successfully grown on graphene (G) nanosheets via the more battery-suitable and cheaper nickel (Ni) catalyst as anode material for high performance lithium ion batteries. Different electrode compositions were investigated until optimal performance was achieved. The primary objective was to investigate this novel SiNW-G nanostructure as a high capacity, high rate capability anode material.

The first electrode composition studied was to see the effect of controlling the SiNWs content, and it was found that too high SiNW amount (above 70 wt%) had higher capacity but very low stability, and too low SiNW content (below 30 wt%) showed superior stability but very low capacity. It was recommended to use 50 wt% SiNW (including Ni mass) with 50 wt% graphene support as a good compromise to achieve good capacity with good stability.

The second electrode composition studied was to see the effect of carbon coating on improving the stability and capacity, and it was found that even though 50wt% SiNW was used higher first cycle discharge was achieved and even higher reversible capacity than in the first study containing 70 wt% SiNW without carbon-coating. But the stability and reversible capacity was still significantly lower than the theoretical maximum of the SiNW-G material.

The third and final study investigated the effect of changing the electrode binder from Sodium carboxymethyl cellulose (NaCMC) to polyacrylonitrile (PAN) followed by pyrolyzing at 550 °C in Argon to achieve dual functionality of binding and conductive coating to enhance the 3D conductivity and stability. The electrochemical testing showed the best performance was achieved with this electrode composition with superior capacity, stability and rate capability.

## **5.1 Recommendation for Future Work**

For future direction, the following can be recommended:

1. Further optimize the material and electrode composition to further improve the long range stability in the order of 500-5000 cycles to be compatible with industrial life time specifications. The following methods may be investigated for that purpose:
  - a. Place a capacity cap as conditioning for the battery to leave some un-reacted Si core which may further stabilize the material. This requires investigation to find the optimal capacity limit that does not sacrifice too much capacity while yielding excellent long range stability.
  - b. Investigate the effect of using higher amount of FEC in the electrolyte and see whether the cost increase is justified by the hoped stability improvement
2. Investigate different types of graphene supports other than by chemical reduction of graphene oxide. Particularly select graphene material with highest possible conductivity.
3. Investigate other carbon coating methods to avoid using Toluene which is a toxic material. Sugar-based carbon coating might be a good start.
4. Try different compositions and testing conditions that allow higher first cycle efficiency, for example by increasing the silicon loading but reducing the voltage range and placing capacity limits as in point 1.

5. Investigate self-standing SiNW-G structure with higher 3D conductivity and stability. Self-standing material without the added inactive mass of copper foil can be very promising for flexibility and higher capacity per mass of the whole electrode (not just per mass of active material).
6. Investigate electrode fabrication with much higher loading than  $0.5 \text{ mg per cm}^{-2}$  for industrial scalability. This may also need investigation of other binders and 3D electrode structure if the pyrolyzing of PAN at high loading can cause material detachment from the copper foil.



## 7. References

1. Scrosati, B. and J. Garche, *Lithium batteries: Status, prospects and future*. Journal of Power Sources, 2010. **195**(9): p. 2419-2430.
2. Divya, K.C. and J. Østergaard, *Battery energy storage technology for power systems—An overview*. Electric Power Systems Research, 2009. **79**(4): p. 511-520.
3. Díaz-González, F., et al., *A review of energy storage technologies for wind power applications*. Renewable and Sustainable Energy Reviews, 2012. **16**(4): p. 2154-2171.
4. Tarascon, J.-M. and M. Armand, *Issues and challenges facing rechargeable lithium batteries*. Nature, 2007. **414**: p. 359-367.
5. Goodenough, J.B. and Y. Kim, *Challenges for rechargeable batteries*. Journal of Power Sources, 2011. **196**(16): p. 6688-6694.
6. Lenovo customer support. *Battery recall*. 2014 [cited 2014 April 7]; Available from: [http://support.lenovo.com/en\\_US/detail.page?DocID=HF004122](http://support.lenovo.com/en_US/detail.page?DocID=HF004122).
7. Sivakkumar, S.R., J.Y. Nerkar, and A.G. Pandolfo, *Rate capability of graphite materials as negative electrodes*. Electrochimica Acta, 2010. **55**(9): p. 3330-3335.
8. Kasavajjula, U., C. Wang, and A.J. Appleby, *Nano- and bulk-silicon-based insertion anodes for lithium-ion secondary cells*. Journal of Power Sources, 2007. **163**(2): p. 1003-1039.
9. Jeong, Y.K., et al., *Hyperbranched beta-Cyclodextrin Polymer as an Effective Multidimensional Binder for Silicon Anodes in Lithium Rechargeable Batteries*. Nano Lett, 2014. **14**(2): p. 864-70.
10. Gowda, S.R., et al., *Three-dimensionally engineered porous silicon electrodes for Li ion batteries*. Nano Lett, 2012. **12**(12): p. 6060-5.
11. Liu, X.H., et al., *Size-Dependent Fracture of Silicon Nanoparticles During Lithiation*. ACS Nano, 2012. **6**(2): p. 1522-1531.
12. Huang, X., et al., *Graphene-based electrodes*. Adv Mater, 2012. **24**(45): p. 5979-6004.
13. Lu, C., et al., *Core-shell CNT-Ni-Si nanowires as a high performance anode material for lithium ion batteries*. Carbon, 2013. **63**: p. 54-60.
14. Gohier, A., et al., *High-rate capability silicon decorated vertically aligned carbon nanotubes for Li-ion batteries*. Adv Mater, 2012. **24**(19): p. 2592-7.
15. Simon, G.K., et al., *Silicon-coated carbon nanofiber hierarchical nanostructures for improved lithium-ion battery anodes*. Journal of Power Sources, 2011. **196**(23): p. 10254-10257.
16. Zu, C.-X. and H. Li, *Thermodynamic analysis on energy densities of batteries*. Energy & Environmental Science, 2011. **4**(8): p. 2614.
17. Treuting, R.G. and S.M. Arnold, *Orientation Habits of Metal Whiskers*. Acta Metallurgica, 1957. **5**: p. 598.
18. Lee, K.T. and J. Cho, *Roles of nanosize in lithium reactive nanomaterials for lithium ion batteries*. Nano Today, 2011. **6**(1): p. 28-41.
19. Chan, C.K., et al., *High-performance lithium battery anodes using silicon nanowires*. Nat Nano, 2008. **3**(1): p. 31-35.
20. Taejin, C., et al., *Synthesis of Si Nanowires by Using Atmospheric Pressure Chemical Vapor Deposition with SiCl<sub>4</sub>*. Journal of the Korean Physical Society, 2011. **59**(21): p. 485.

21. Schmidt, V., et al., *Silicon Nanowires: A Review on Aspects of their Growth and their Electrical Properties*. *Advanced Materials*, 2009. **21**(25-26): p. 2681-2702.
22. Wen, C.Y., et al., *Structure, Growth Kinetics, and Ledge Flow during Vapor–Solid–Solid Growth of Copper-Catalyzed Silicon Nanowires*. *Nano Letters*, 2009. **10**(2): p. 514-519.
23. Zhang, R.-Q., Y. Lifshitz, and S.-T. Lee, *Oxide-Assisted Growth of Semiconducting Nanowires*. *Advanced Materials*, 2003. **15**(7-8): p. 635-640.
24. Tan, T.Y., et al., *A model for growth directional features in silicon nanowires*. *Applied Physics A: Materials Science & Processing*, 2002. **74**(3): p. 423-432.
25. Chan, C.K., et al., *Solution-Grown Silicon Nanowires for Lithium-Ion Battery Anodes*. *ACS Nano*, 2010. **4**(3): p. 1443-1450.
26. Ge, M., et al., *Review of porous silicon preparation and its application for lithium-ion battery anodes*. *Nanotechnology*, 2013. **24**(42): p. 422001.
27. Ban, V.S. and S.L. Gilbert, *The chemistry and transport phenomena of chemical vapor deposition of silicon from SiCl<sub>4</sub>*. *Journal of Crystal Growth*, 1975. **31**: p. 284-289.
28. Uesawa, N., et al., *Gas-Phase Synthesis of Rough Silicon Nanowires via the Zinc Reduction of Silicon Tetrachloride*. *Journal of Physical Chemistry C*, 2010. **114**: p. 4291-4296.
29. Mai, Y.J., et al., *Graphene anchored with nickel nanoparticles as a high-performance anode material for lithium ion batteries*. *Journal of Power Sources*, 2012. **209**: p. 1-6.
30. Zhu, X.-J., et al., *Reduced graphene oxide and nanosheet-based nickel oxide microsphere composite as an anode material for lithium ion battery*. *Electrochimica Acta*, 2012. **64**: p. 23-28.
31. Nithya, C. and S. Gopukumar, *Reduced graphite oxide/nano Sn: a superior composite anode material for rechargeable lithium-ion batteries*. *ChemSusChem*, 2013. **6**(5): p. 898-904.
32. Zhang, L.L., Z. Xiong, and X.S. Zhao, *A composite electrode consisting of nickel hydroxide, carbon nanotubes, and reduced graphene oxide with an ultrahigh electrocapacitance*. *Journal of Power Sources*, 2013. **222**: p. 326-332.
33. Chockla, A.M., et al., *Influences of Gold, Binder and Electrolyte on Silicon Nanowire Performance in Li-Ion Batteries*. *Journal of Physical Chemistry C*, 2012. **116**(34): p. 18079-18086.
34. Massalski, T.B., et al., *Binary Alloy Phase Diagrams*. 2nd ed. Vol. 1-3. 1990, Materials Park, Ohio: ASM International.
35. Wanger, R.S., et al., *Study of the Filamentary Growth of Silicon Crystals from the Vapor*. *Journal of Applied Physics*, 1965. **35**(10): p. 2993-3000.
36. Kamins, T.I., et al., *Chemical vapor deposition of Si nanowires nucleated by TiSi<sub>2</sub> islands on Si*. *Applied Physical Letters*, 2000. **76**(5): p. 562-567.
37. Nash, P. and A. Nash, *The Ni-Si (Nickel-Silicon) System*. *Bulletin of Alloy Phase Diagrams*, 1987. **9**(1): p. 6-14.
38. Zhang, Y., et al., *Synthesis of thin Si whiskers (nanowires) using SiCl<sub>4</sub>*. *Journal of Crystal Growth*, 2001. **226**: p. 185-191.
39. Xu, C., et al., *Graphene-based electrodes for electrochemical energy storage*. *Energy & Environmental Science*, 2013. **6**(5): p. 1388.
40. Han, S., et al., *Graphene: a two-dimensional platform for lithium storage*. *Small*, 2013. **9**(8): p. 1173-87.

41. C. Liu, F.L., L. P. Ma and H. M. Cheng, *Advanced materials for energy storage*. *Advanced Materials*, 2010. **22**: p. E28–62.
42. Wang, B.L., X.; Zhang, X.; Luo, B.; Jin, M.; Liang, M.; Dayeh S. A.; Picraux, S. T.; Zhi, L., *Adaptable Silicon-Carbon Nanocables Sandwiched between Reduced Graphene Oxide Sheets as Lithium Ion Battery Anodes*. *ACS Nano*, 2013. **7**(2): p. 1437-1445.
43. Luo, J., et al., *Crumpled Graphene-Encapsulated Si Nanoparticles for Lithium Ion Battery Anodes*. *The Journal of Physical Chemistry Letters*, 2012. **3**(13): p. 1824-1829.
44. Wang, X.L. and W.Q. Han, *Graphene enhances Li storage capacity of porous single-crystalline silicon nanowires*. *ACS Appl Mater Interfaces*, 2010. **2**(12): p. 3709-13.
45. Chabot, V., et al., *Graphene wrapped silicon nanocomposites for enhanced electrochemical performance in lithium ion batteries*. *Electrochimica Acta*, 2014. **130**(0): p. 127-134.
46. Zhou, M., et al., *Graphene/carbon-coated Si nanoparticle hybrids as high-performance anode materials for Li-ion batteries*. *ACS Appl Mater Interfaces*, 2013. **5**(8): p. 3449-55.
47. Hummers, W.S. and R.E. Offeman, *Preparation of Graphitic Oxide*. *Journal of the American Chemical Society*, 1958. **80**(6): p. 1339-1339.
48. Chun, M.-J., et al., *Bicontinuous structured silicon anode exhibiting stable cycling performance at elevated temperature*. *RSC Advances*, 2013. **3**(44): p. 21320.
49. Oehlschlaeger, M.A., D.F. Davidson, and R.K. Hanson, *Thermal decomposition of toluene: Overall rate and branching ratio*. *Proceedings of the Combustion Institute*, 2007. **31**(1): p. 211-219.
50. Wilson, A.M. and J.R. Dahn, *Lithium Insertion in Carbons Containing Nanodispersed Silicon*. *Journal of the Electrochemical Society*, 1995. **142**(2): p. 326-332.
51. Carter, D.B.W.a.C.B., *Transmission Electron Microscopy - A Textbook for Materials Science*. 2nd ed. 2009: Springer.
52. L. V. Azaroff, R.K., N. Kato, R. J. Weiss, A. Wilson, and R. Young, *X-ray Diffraction*. 1974: McGraw-Hill.
53. Morris, M.C.M., Howard F.; Evans, Eloise H.; Paretzkin, Boris; de Groot, Johan H.; Hubbard, Camden R., et al. , *Standard X-ray Diffraction Powder Patterns: Section 13. Data for 58 substances*. . UNT Libraries Government Documents, 1976
54. Gardiner, D.J., *Practical Raman Spectroscopy*. 1989: Springer - Verlag.
55. Hassan, F.M., et al., *Engineered Si Electrode Nanoarchitecture: A Scalable Postfabrication Treatment for the Production of Next-Generation Li-Ion Batteries*. *Nano Letters*, 2013. **14**(1): p. 277-283.
56. Etacheri, V., et al., *Effect of fluoroethylene carbonate (FEC) on the performance and surface chemistry of Si-nanowire Li-ion battery anodes*. *Langmuir*, 2012. **28**(1): p. 965-76.
57. Reddy, T.B., *Linden's Handbook of Batteries*. 4th ed. 2011: McGraw-Hill Education.
58. Lavin-Lopez, M.P., et al., *Synthesis and characterization of graphene: influence of synthesis variables*. *Physical Chemistry Chemical Physics*, 2014. **16**(7): p. 2962-2970.
59. Fu, K., et al., *Effect of CVD carbon coatings on Si@CNF composite as anode for lithium-ion batteries*. *Nano Energy*, 2013. **2**(5): p. 976-986.
60. Yen, Y.-C., et al., *Study on Solid-Electrolyte-Interphase of Si and C-Coated Si Electrodes in Lithium Cells*. *Journal of The Electrochemical Society*, 2009. **156**(2): p. A95.
61. Zhou, G., F. Li, and H.-M. Cheng, *Progress in flexible lithium batteries and future prospects*. *Energy & Environmental Science*, 2014.

62. Thakur, M., et al., *Inexpensive method for producing macroporous silicon particulates (MPSPs) with pyrolyzed polyacrylonitrile for lithium ion batteries*. Sci Rep, 2012. **2**: p. 795.
63. Ge, M., et al., *Porous doped silicon nanowires for lithium ion battery anode with long cycle life*. Nano Lett, 2012. **12**(5): p. 2318-23.